



**Calhoun: The NPS Institutional Archive**  
**DSpace Repository**

---

Theses and Dissertations

1. Thesis and Dissertation Collection, all items

---

1962-12

# Stability characteristics of quasi-barotropic flow.

Song, Rak To.

Monterey, California. Naval Postgraduate School

---

<http://hdl.handle.net/10945/20349>

---

*Downloaded from NPS Archive: Calhoun*



Calhoun is the Naval Postgraduate School's public access digital repository for research materials and institutional publications created by the NPS community. Calhoun is named for Professor of Mathematics Guy K. Calhoun, NPS's first appointed -- and published -- scholarly author.

**Dudley Knox Library / Naval Postgraduate School**  
**411 Dyer Road / 1 University Circle**  
**Monterey, California USA 93943**

<http://www.nps.edu/library>

STABILITY CHARACTERISTICS  
OF QUASI-BAROTROPIC FLOW

SONG, RAK TO

LIBRARY  
U.S. NAVAL POSTGRADUATE SCHOOL  
MONTEREY, CALIFORNIA





STABILITY CHARACTERISTICS  
of  
QUASI-BAROTROPIC FLOW

\* \* \* \* \*

SONG, RAN TO



STABILITY CHARACTERISTICS

OF

QUASI-BAROTROPIC FLOW

by

Son,, Rak To  
//

Lieutenant, Republic of Korea Navy

Submitted in partial fulfillment of  
the requirements for the degree of

MASTER OF SCIENCE  
IN

METEOROLOGY

United States Naval Postgraduate School  
Monterey, California

1 5 6 2





LIBRARY  
U.S. NAVAL POSTGRADUATE SCHOOL  
MONTEREY, CALIFORNIA

STABILITY CHARACTERISTICS

of

QUASI-BAROTROPIC FLOW

by

Song, Rak To

This work is accepted as fulfilling  
the thesis requirements for the degree of

MASTER OF SCIENCE

IN

METEOROLOGY

from the

United States Naval Postgraduate School



## ABSTRACT

The stability characteristics of several anisotropic models (the divergent, one-parameter and the stratiform models) are investigated for various symmetrical zonal wind fields, including single-jet and double-jet profiles. Two different approximations are used for the amplitude of the perturbation stream function, one of which is based on a method of finite differences, and the second on a representation by a finite Fourier series. The results of the two methods are compared to one another as well as to those of previous investigators.

The second-order effects of the unstable perturbations on a double-jet zonal flow are determined from the convergence of meridional transport of momentum by the eddies. It is shown that this type of zonal wind profile changes to a single-jet mean flow in a few days.

The writer is indebted to Professor George J. Haltiner of the Department of Meteorology and Oceanography at the United States Naval Postgraduate School for having suggested the topic and for guidance during its development. He is also indebted to Assistant Professor Robert J. Renard for proofreading of the manuscript.



# TABLE OF CONTENTS

Section	Title	Page
1.	Introduction	1
2.	Stability properties of the divergent, one-parameter model	3
A.	Basic equations	3
B.	Method of finite differences	6
	Part I. $N = 5$ (or $d = D/6$ )	6
	Part II. $N = 7$ (or $d = D/8$ )	14
C.	Fourier series method	18
3.	Stability properties of the stratified model	23
4.	Momentum changes	26
5.	Summary	31
6.	Bibliography	37



# LIST OF ILLUSTRATIONS

Figure	Page
1. The zonal wind channel showing the four subdivisions	1
2. The profiles of the zonal wind	33
3-6. The imaginary part, $c_i$ , of the solution to equation (2.12) as a function of wavelength for $D = 2000$ , 3000, 4000, and 6000 km, respectively; and for $\bar{U} = B(1 - \cos \frac{2\pi}{D}y)$ , $d = \frac{D}{6}$ , and $B = 30 \text{ m sec}^{-1}$	34-37
7. The imaginary part, $c_i$ , of the solution to equation (2.12) as a function of the meridional width $D$ for $L = 5000 \text{ km}$ , $\bar{U} = B(1 - \cos \frac{2\pi}{D}y)$ , $d = \frac{D}{6}$ , and $B = 30 \text{ m sec}^{-1}$	38
8-10. The imaginary part, $c_i$ , of the solution to equation (2.12) as a function of wavelength for $D = 2000$ , 4000, and 6000 km, respectively; and for $\bar{U}_0 = 2B$ , $\bar{U}_1 = B$ , $\bar{U}_2 = \frac{B}{2}$ , $d = \frac{D}{6}$ , and $B = 30 \text{ m sec}^{-1}$	39-41
11-12. The imaginary part, $c_i$ , of the solution to equation (2.12) as a function of wavelength for $D = 2000$ and 4000 km, respectively; and for $\bar{U} = B(\sin \frac{\pi}{D}y + \sin \frac{3\pi}{D}y)$ , $d = \frac{D}{6}$ , and $B = 40 \text{ m sec}^{-1}$	42-43
13-15. The imaginary part, $c_i$ , of the solution to equation (2.12) as a function of wavelength for $D = 2000$ , 4000, and 6000 km, respectively; and for $\bar{U} = B(\cos \frac{4\pi}{D}y - \cos \frac{2\pi}{D}y)$ , $d = \frac{D}{6}$ , and $B = 30 \text{ m sec}^{-1}$	44-46
16. The zonal wind channel showing the eight subdivisions.	44
17-19. The imaginary part, $c_i$ , of the solution to equation (2.16) as a function of wavelength for $D = 2000$ , 4000, and 6000 km, respectively; and for $\bar{U} = B(1 - \cos \frac{2\pi}{D}y)$ , $d = \frac{D}{8}$ , and $B = 30 \text{ m sec}^{-1}$	47-49
20-21. The imaginary part, $c_i$ , of the solution to equation (2.16) as a function of wavelength for $D = 2000$ and 4000 km, respectively; and for $\bar{U} = B(\sin \frac{\pi}{D}y + \sin \frac{3\pi}{D}y)$ , $d = \frac{D}{8}$ , and $B = 40 \text{ m sec}^{-1}$	50-51





- 22-24. The imaginary part,  $c_i$ , of the solution to equation (2.22) as a function of wavelength for  $D = 2000$ , 4000, and 6000 km, respectively; and for  $\bar{U} = B(1 - \cos \frac{2\pi}{D} y)$ ,  $N = 5$ , and  $B = 30 \text{ m sec}^{-1}$  52-54
- 25-27. The imaginary part,  $c_i$ , of the solution to equation (2.23) as a function of wavelength for  $D = 2000$ , 4000, and 6000 km, respectively; and for  $\bar{U} = B(1 - \cos \frac{2\pi}{D} y)$ ,  $N = 7$ , and  $B = 30 \text{ m sec}^{-1}$  55-57
- 28-30. The imaginary part,  $c_i$ , of the solution to equation (2.23) as a function of wavelength for  $D = 2000$ , 4000, and 6000 km, respectively; and for  $\bar{U} = B(1 - \cos \frac{4\pi}{D} y)$ ,  $N = 5$ , and  $B = 30 \text{ m sec}^{-1}$  58-60
- 31-32. The imaginary part,  $c_i$ , of the solution to equation (3.4) as a function of wavelength for  $D = 2000$  and 4000 km, respectively; and for  $\bar{U} = B(1 - \cos \frac{2\pi}{D} y)$ , stratified model,  $N = 5$ , and  $B = 30 \text{ m sec}^{-1}$  61-62
33. The function  $M(y)$  as defined by equation (4.3) 63
- 34-35. The distribution of zonal wind as a function of time computed from equation (4.3) with  $\beta = \beta_{45}$ ,  $q = 0$ ,  $D = 3000 \text{ km}$ ,  $L = 2000 \text{ km}$ ,  $B = 30 \text{ m sec}^{-1}$ ,  $A_1$  corresponds to  $5 \text{ m sec}^{-1}$  ( $A_1 = 1.55 \times 10^6 \text{ m}^2 \text{ sec}^{-1}$ ) and with  $A_3 = 0$  and  $A_3 = A_1$ , respectively 64-65
36. The distribution of zonal wind as a function of time computed from equation (4.3) with the same parameters as in fig. 35, except  $D = 6000 \text{ km}$  and  $L = 4000 \text{ km}$  66



# TABLE OF SYMBOLS AND ABBREVIATIONS

$A_1$ & $A_3$	Amplitudes of the wave components of the initial perturbation stream function
$A(p)$	The empirical function describing the vertical variation of the horizontal wind around the 500-mb level
$B$	Amplitude of mean zonal wind profile
$c$	Phase velocity
$c_r$	The real part of the phase velocity
$c_i$	The imaginary part of the phase velocity
$D$	The meridional width of the basic channel
$d$	Mesh length of subdivision of the channel, $d = \frac{D}{N+1}$
$e$	The base of Napierian logarithms
$f$	The Coriolis parameter
$f_0$	A standard value of $f$
$g''$	Acceleration of gravity corrected for compressibility
$H$	Thickness of the stratified layer
$i$	The unit imaginary number
$\hat{i}$	Unit vector in the x-direction
$\hat{k}$	Unit vector directed upward
$L$	Wavelength
$N$	Number of the points subdividing the basic channel; also, the maximum number of Fourier series terms
$n$	An integer index
$p$	Pressure
$q^2$	A measure of the intensity of divergence, $q^2 = \frac{f_0}{\sigma} \frac{\partial G}{\partial p} \frac{dA}{dp}$ for the one-parameter model; also $q^2 = \frac{f(\nabla^2 \psi + \bar{\psi})}{g'' H}$ for the stratified model



$t$	Time
$\bar{u}$	Mean zonal wind velocity
$u$	Component of wind velocity in the $x$ -direction
$v$	Component of wind velocity in the $y$ -direction
$\mathbf{V}$	Horizontal non-divergent wind velocity, $\mathbf{V} = \mathbf{k} \times \nabla \psi$
$\bar{\mathbf{V}}$	$\bar{\mathbf{V}} = \bar{u} \mathbf{i}$
$x$	Coordinate toward the east
$y$	Coordinate toward the north
$\alpha$	Specific volume
$\beta$	Rossby parameter
$\beta_{45}$	Rossby parameter at 45N
$\theta$	Potential temperature
$\lambda$	$\lambda = \frac{\pi}{D}$
$\mu$	Wave number, $\mu = \frac{2\pi}{L}$
$\sigma$	A measure of static stability, $\sigma = - \left( \frac{\alpha}{\theta} \right) \frac{\partial \theta}{\partial p}$
$\phi(y)$	Amplitude of the perturbation stream function
$\Phi_n$	Amplitudes at the positions indicated by $n$ ; also the amplitudes of the wave components of perturbation stream function
$\psi$	The stream function
$\nabla$	Horizontal gradient operator on a constant-pressure surface
$\nabla^2$	Horizontal Laplacian operator on a constant-pressure surface
$'$	Perturbation quantity
$\sum$	Summation over an indicated range of indices



## 1. Introduction.

The barotropic model, conceived by Rossby more than two decades ago, has played a role in numerical forecasting far beyond expectations. When operational forecasting with the barotropic model began in the early '50's, it was expected that the more sophisticated baroclinic types would soon replace the former; however, difficulties with these models, together with further improvements in the barotropic model, have caused continued interest in the latter.

One aspect of barotropic flow which has been investigated in some detail is the dynamic stability of zonal currents, notably by Kuo [1] and Eliassen [2] for non-divergent flow, and for the divergent case by Wiin-Nielsen [3].

In the first part of this paper, the stability properties of various barotropic models will be studied by two different approaches, namely a finite-difference method and a finite Fourier-series method. A variety of zonal wind profiles will be considered, including single and double wind-speed maxima. The results of the two methods are compared to one another as well as to those of previous investigators.

The performance of the numerical prediction models, when integrated over periods of time up to several days, weeks, or even more, has been recently of special interest. Thompson [4] has developed a heuristic theory of long-period velocity variations in barotropic flow. In particular, it was shown from this theory that a double-jet maxima in the zonal wind profile





develops in two or three ways from an initial single-jet. Such conditions seem to be characteristic of certain types of atmospheric currents when a block occurs. This theory is based upon the interaction between eddies and the mean flow.

Wiin-Nielsen [3] has recently shown that the splitting of a single isotach maximum in the meridional wind profile (single jet) into two maxima (double jet) is a dynamical consequence of the convergence of meridional momentum transport by the eddies, provided there is barotropic instability in an initial flow. It may be noted also that the time scale of the changes in the mean zonal flow is the same in both theories, as may be expected, since the physical model is basically the same.

The second part of this paper is devoted to a study of second-order effects of the perturbations on mean zonal flow which has double maxima.



## 2. Stability properties of the two-dimensional, one-parameter model

### A. Basic equations.

The vorticity equation for the two-dimensional, one-parameter model (or equivalent barotropic model) may be written in the following form due to Hines-Nielsen [1] :

$$\frac{\partial}{\partial t}(\nabla^2 \psi) + \mathbf{V} \cdot \nabla (\nabla^2 \psi + f) = q^2 \frac{\partial \psi}{\partial t} \quad (2.1)$$

where  $\psi$  is the stream function ;

$$\mathbf{V} = \mathbf{U} \times \nabla \psi, \quad \text{the horizontal mean velocity vector}$$

and  $q^2 = \frac{f_0^2}{\sigma^2} \frac{d\sigma}{dp} \frac{dH}{dp}$ . (2.2)

In equation (2.2)  $\sigma = -(\frac{g}{\theta}) \frac{\partial \theta}{\partial p}$  is a measure of static stability,  $f_0$  a standard value of the Coriolis parameter, and  $A(p)$  is an empirical function describing the vertical variation of the horizontal wind near the level where the vorticity equation is applied (500 mb), namely

$$\mathbf{V}(x, y, p, t) = A(p) \mathbf{V}_0(x, y, t). \quad (2.3)$$

By applying the perturbation method, the geopotential equation (2.1) may be written in the form

$$\nabla^2 \frac{\partial \psi'}{\partial t} + \bar{U} \frac{\partial}{\partial x} (\nabla^2 \psi') + \frac{\partial \psi'}{\partial x} \left( \beta - \frac{d^2 \bar{U}}{dy^2} \right) = q^2 \frac{\partial \psi'}{\partial t} \quad (2.4)$$

where  $\bar{U}(y) = -\frac{\partial \bar{\psi}}{\partial y}$  is the mean zonal wind velocity, and  $\psi'$  is the perturbation stream function.

The perturbation stream function will be considered in the form

$$\psi'(x, y, t) = \phi(y) e^{i\mu(x-ct)} \quad (2.5)$$



Substituting (2.5) into (2.4) yields the result

$$(\bar{U} - c) \left[ \frac{d^2 \phi}{dy^2} - \mu^2 \phi \right] + \left[ \beta - \frac{d^2 \bar{U}}{dy^2} + q^2 c \right] \phi = 0 \quad (2.6)$$

In (2.5)  $\mu = \frac{2\pi}{L}$  (a real quantity) and  $c$ , the phase velocity, may be complex, that is

$$c = c_r + i c_i \quad (2.7)$$

If, in (2.7),  $c_i \neq 0$  the amplitude will be an exponential function of time  $t$  and the wave is said to be unstable.

For  $c_i > 0$ , the amplitude will increase with time; if, on the other hand,  $c_i < 0$ , the wave will be damped.

Equation (2.6) is a second-order differential equation and is to be solved for certain boundary conditions. Since disturbances in zonal currents are normally bounded to the north and south, the simplest type of suitable boundary condition may be written in the form

$$\phi(0) = \phi(D) = 0 \quad (2.8)$$

corresponding to rigid boundaries at  $y = 0$  and  $y = D$ , where the perturbation stream function is assumed to vanish.

Now, as an eigen-value problem, we are interested in the relationship between  $c$ ,  $\mu$  and other pertinent parameters for which there exists solutions of the system (2.6) and (2.8).

Since the basic current is a function of  $y$ , the mathematical problem here is rather complicated; and generally we cannot find, even for simple functions  $\bar{U}(y)$ , an analytical expression for the perturbation amplitude  $\phi(y)$ . Hence it appears logical to attempt



solution by a finite-difference method or a finite Fourier series method which can be adapted to the particular boundary conditions (2.8).





## B. Method of Finite Differences.

In the atmosphere, velocity profiles of the westerlies generally have appreciable symmetry with respect to some latitude. For simplicity, particular symmetric profiles, especially single-jet and double-jet profiles, will be discussed.

Since only symmetric wind profiles and boundary conditions are considered, symmetry of the amplitude  $\phi(y)$  of the perturbation stream function may be expected. Therefore, only half of the wind belt need be considered.

In so doing we shall consider the function  $\phi(y)$  as given by its values  $\phi_n$  at  $N$  points in the interval,  $0 \leq y \leq D$ , such that the interval is divided by these points into  $N + 1$  equal parts, each of the length  $d = \frac{D}{N+1}$  (Figure 1). The meridional derivatives of  $\phi(y)$  will be approximated by the corresponding quotients of centered differences such as

$$\left(\frac{d^2\phi}{dy^2}\right)_n = \frac{\phi_{n+1} + \phi_{n-1} - 2\phi_n}{d^2} \dots \quad (2.5)$$

In general it may be expected that the approximation of the derivatives by this difference ratio will give better results as the value of  $N$  increases, although the mathematical analysis becomes more tedious. However, for simplicity in this section only, the cases of  $N = 5$  and  $N = 7$  will be considered.

Part I.  $N = 5$ , (or  $d = \frac{D}{6}$ ).

By combining (2.2) and the given boundary conditions (2.8), the derivatives of the perturbation amplitude at each point (Fig. 1) can be written in the form



$$\begin{aligned}
\left(\frac{d^2\phi}{dy^2}\right)_0 &= \frac{2\phi_1 - 2\phi_0}{d^2} \\
\left(\frac{d^2\phi}{dy^2}\right)_1 &= \frac{\phi_2 + \phi_0 - 2\phi_1}{d^2} \\
\left(\frac{d^2\phi}{dy^2}\right)_2 &= \frac{\phi_1 - 2\phi_2}{d^2}
\end{aligned} \tag{2.10}$$

where the subscripts 0, 1, and 2 represent the values at  $y = \frac{D}{2}$ ,  $y = \frac{2}{3}D$ , and  $y = \frac{5}{6}D$ , respectively.

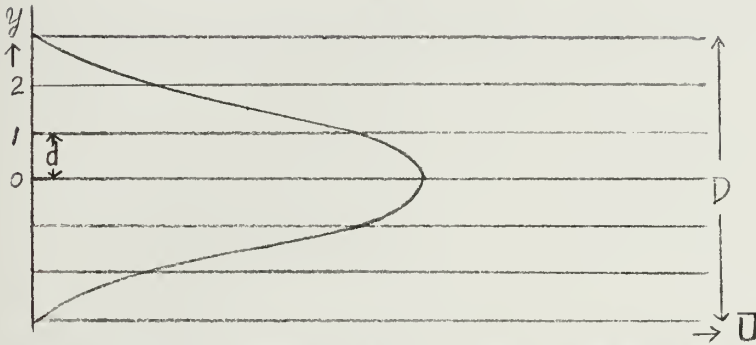


Fig. 1. The zonal wind channel showing the six divisions.

Since (2.6) must be satisfied at each point of fig. 1, the following set of equations with the use of (2.10) are obtained:

$$\begin{aligned}
[(\bar{U}_0 - c)(-2 - \mu^2 d^2) + d^2(\beta - \bar{U}_0'') + d^2 q^2 c] \phi_0 + 2(\bar{U}_0 - c) \phi_1 &= 0 \\
(\bar{U}_1 - c) \phi_0 + [(\bar{U}_1 - c)(-2 - \mu^2 d^2) + d^2(\beta - \bar{U}_1'') + d^2 q^2 c] \phi_1 + (\bar{U}_1 - c) \phi_2 &= 0 \quad (2.11) \\
(\bar{U}_2 - c) \phi_1 + [(\bar{U}_2 - c)(-2 - \mu^2 d^2) + d^2(\beta - \bar{U}_2'') + d^2 q^2 c] \phi_2 &= 0
\end{aligned}$$

where  $\bar{U}_0$ ,  $\bar{U}_1$ ,  $\bar{U}_2$ ,  $\bar{U}_0''$ ,  $\bar{U}_1''$  and  $\bar{U}_2''$  are the values of  $\bar{U}$  and  $\bar{U}''$  at  $y_0$ ,  $y_1$  and  $y_2$ , respectively. Here the double prime represents the second derivative with respect to  $y$ . For a known initial zonal wind profile, (2.11) constitutes a system of three equations in three unknowns  $\phi_0$ ,  $\phi_1$ , and  $\phi_2$ . Since the system (2.11) is homogeneous, the possible values of  $c$  may now be obtained from the condition that the determinant of the system (2.11) must vanish in order to have non-trivial solutions. This condition leads to the so-called frequency equation in the form:



$$\begin{aligned}
& C^3[h(h^2-3)] + C^2[h\{(P_1+P_2)h + (U_1+U_2)(1-\gamma h)\} \\
& + (h^2-1)(P_0-U_0\gamma) + 2h(U_1+U_2) - 2(P_2-U_2\gamma)] + C[h\{U_1U_2(\gamma^2 \\
& -1) + P_1P_2 - \gamma(P_1U_2+P_2U_1)\} + \{h(P_1+P_2) + (U_1+U_2)(1-\gamma h)\} \\
& \{P_0-U_0\gamma\} - 2hU_0U_1 + 2(U_1+U_2)(P_2-U_2\gamma)] + [U_1U_2(\gamma^2-1) \\
& + P_1P_2 - \gamma(P_1U_2+P_2U_1)\} \{P_0-U_0\gamma\} - 2U_0U_1(P_2-U_2\gamma)] = 0
\end{aligned} \quad (2.12)$$

where

$$P_0 = d^2(\beta - U_0''),$$

$$P_1 = d^2(\beta - U_1''),$$

$$P_2 = d^2(\beta - U_2''),$$

$$\gamma = 2 + u^2 d^2,$$

and  $h = \gamma + d^2 q^2$ .

It should be noted that  $\beta$  and  $q$  were assumed constant in deriving (2.12). Since the frequency equation (2.12) is a cubic equation in the phase velocity  $c$ , in general there exists three roots, which may include a pair of complex roots. The imaginary part of the phase velocity,  $c_i$ , which is necessary for unstable perturbations, will be considered of primary interest in this paper.

The frequency equation (2.12) has been solved numerically for a number of cases with a Control-Data-Corporation 1604 computer, using the so-called Muller method [6] for finding the roots of polynomials. For each of the initial wind profiles and meridional distances between the rigid boundaries, the solution was obtained for various zonal wavelengths ( $L = \frac{2\pi}{\mu}$ ),



keeping  $\beta$  and  $q$  constant. Then the effects of  $\beta$  and divergence  $q$  were tested by making each of these parameters zero in a series of computations.

It is of special interest to consider the stability problem for those types of initial wind profiles which are not only symmetric with respect to the center of the channel, but also frequently found in the actual atmosphere.

#### Example 1. Single-jet basic current.

For the first example, the zonal wind profile will be considered in the form

$$U = B \left( 1 - \cos \frac{2\pi y}{D} \right) \quad (2.13)$$

which is shown as curve (1) in figure 2. Inserting (2.13) into (2.12) and varying the pertinent parameters  $B$ ,  $D$ ,  $f$ , and  $q$  leads to the results given in figures 3, 4, 5, 6, and 7.

In figure 3 the meridional width of the channel,  $D$ , is 2000 km and the maximum zonal speed at the center of the channel is  $60 \text{ m sec}^{-1}$  ( $B = 30 \text{ m sec}^{-1}$ ). This case corresponds to a rather intense single-jet wind profile, which is often found at the 500-mb level. The abscissa in the figure is zonal wavelength in units of thousands of km, while the ordinate is the imaginary part of the phase velocity  $c_i$ . The figure contains five curves corresponding to the cases: curve (1)  $\beta = 0$ ,  $q = 0$ ; (2)  $\beta = \beta_{45}$ ,  $q = 0$ ; (3)  $\beta = \beta_{45}$ ,  $q^2 = 0.5 \times 10^{-12} \text{ m}^{-2}$ ; (4)  $\beta = \beta_{45}$ ,  $q^2 = 1.0 \times 10^{-12} \text{ m}^{-2}$ ; and (5)  $\beta = \beta_{45}$ ,  $q^2 = 1.5 \times 10^{-12} \text{ m}^{-2}$ .

Here  $\beta_{45}$  represents the meridional derivative of the Coriolis parameter at latitude  $45^\circ\text{N}$  which has the value  $1.618 \times 10^{-11} \text{ m}^{-1} \text{ sec}^{-1}$ .





By comparing the two first curves, it is seen that the parameter  $\beta$  has a stabilizing influence on the perturbation in the sense that the magnitude of  $c_i$  is smaller and the band of wavelengths for which instability occurs is more narrow for  $\beta \neq 0$  than in the case of  $\beta = 0$ . Moreover, by comparing the first two curves with the last three curves it is also seen that  $q$ , which is a measure of the intensity of the divergence implied by this model, has further stabilizing effects. Therefore, the divergent, one-parameter model is more stable than the non-divergent model. Furthermore, the stabilizing effects of  $\beta$  and the divergence term are much more pronounced for relatively longer wavelengths in the previously unstable bands. Thus the maximum  $c_i$ 's occur at shorter wavelengths for  $\beta \neq 0$  and  $q \neq 0$ , than in the case of  $\beta = q = 0$ .

It should be noted in this figure that the instability occurs only for the intermediate zonal wavelengths (in this case 2000-8000 km for  $\beta = q = 0$ ), which is in agreement with the average length of observed synoptic waves. In other words, for sufficiently short and long wavelengths, instability does not exist. This is similar to the results of the two-level baroclinic instability discussed by Thompson [7].

The preceding results are nicely verified by figures 4, 5, and 6, which contain similar computations with the meridional widths, 3000, 4000, and 6000 km, respectively. The additional information shown in these figures is that the band of unstable wavelengths is shifted toward longer wavelengths such that  $c_i$  becomes maximum at  $\frac{L}{D} \approx 2.0$  for  $\beta = q = 0$ ; and also the



magnitude of the imaginary root  $c_i$  does not change with  $D$  in this case. This result is completely consistent with Eliasson [2]. Moreover, it may be noted that the stabilizing effects of  $\beta$  and  $q$  are generally more pronounced with increasing  $D$ ; thus the waves are more stable in the divergent model with increasing width of the channel. For example, with  $D = 4000$  km, all wavelengths are stable in the case of  $\beta = \beta_{45}$  and  $q^2 = 1.5 \times 10^{-12} \text{ m}^{-2}$ , and only the waves in a narrow band around 5000 km are unstable for  $\beta = \beta_{45}$  and  $q^2 = 1.0 \times 10^{-12} \text{ m}^{-2}$ . For  $D = 6000$  km, only the case,  $\beta = 0$  and  $q = 0$ , is unstable.

Figure 7 contains five curves giving the imaginary root  $c_i$  as a function of the meridional width,  $D$ , for a fixed value of the zonal wavelength,  $L = 5000$  km.

Example 2.

For the second profile, it will be assumed that

$$\begin{aligned}\bar{U}_0 &= 2B \\ \bar{U}_1 &= B \\ \bar{U}_2 &= \frac{B}{2}\end{aligned}\tag{2.14}$$

where  $B = 30 \text{ m sec}^{-1}$ .

Using the finite-difference approximation for the derivatives of zonal wind speed with respect to  $y$  yields

$$\begin{aligned}U_0'' &= -\frac{2B}{d^2} \\ U_1'' &= \frac{B}{2d^2} \\ U_2'' &= 0\end{aligned}\tag{2.15}$$



Inserting (2.14) and (2.15) into (2.12) and performing the necessary computations leads to the results shown in figures 8, 9, and 10, corresponding to  $D = 2000$ ,  $4000$ , and  $6000$  km, respectively.

It is readily seen that the results of the instability features for this profile are quite similar to those of the first profile, which is to be expected since the two profiles are similar. By comparing with example 1, the main difference in this wind profile is that the maximum values of  $c_i$  occur at  $\frac{L}{D} = 1.5$  for  $\beta = q = 0$ , and also the band of unstable wavelengths shifts to slightly shorter wavelengths than for the previous basic current. Moreover, when  $D = 4000$  km, it is seen that all waves are stable in the last two cases. Hence it may be concluded that the stabilizing effects of  $\beta$  and  $q$  in this basic current are much more pronounced with increasing  $D$  than in example 1.

### Example 3. Double-jet basic current.

In preceding two examples, a stability study was given for symmetric single-jet wind profiles. Now in this example, we will investigate the stability characteristics of the symmetric double-jet wind profile, represented by the expression

$$U = B \left( \sin \frac{\pi}{D} y + \sin \frac{3\pi}{D} y \right) \quad (2.16)$$

which is shown as curve (2) in figure 2.

Inserting (2.16) into (2.12) and performing the series of computations yields the results shown in figures 11 and 12, corresponding to  $D = 2000$  and  $4000$  km, respectively.

Contrary to the results of example 1, it is seen that  $\beta$  and  $q$  do not show the stabilizing influence for all wavelengths.



For relatively longer wavelengths (longer than the wavelength at which the maximum of  $c_1$  for  $\beta = q = 0$  occurs), the  $\beta$ -effect has a destabilizing influence on the perturbations in such a way that the magnitude of  $c_1$  is greater for  $\beta \neq 0$  than for  $\beta = 0$ . Also the band of wavelengths for which instability occurs is broader for  $\beta \neq 0$ . Furthermore, for these longer wavelengths the effect of  $q$ , a measure of divergence, is to further increase the instability of the waves similarly to the  $\beta$ -effect.

It should be noted that two maxima of  $c_1$  occurs for  $D = 4000$  km, when  $\beta \neq 0$  and  $q \neq 0$ ; and that the waves are much more unstable when the meridional width  $D$  is increased. Hence the divergent, one-parameter model in the double-jet wind profile appears more unstable than the non-divergent model, which is opposite to the results for the single-jet profile.

It should be mentioned here that the subdivision of the basic channel by finite differences into 6 mesh lengths corresponding to the case  $N = 5$ , is probably a cruder representation for the double-jet basic current than for the single-jet; hence the results for the former may be expected to be less accurate due to larger truncation errors. This aspect will be considered again in Part II.

Example 4. 
$$\bar{U} = B \left( \cos \frac{4\pi}{D} y - \cos \frac{2\pi}{D} y \right). \quad (2.17)$$

This profile has easterly wind components to the north and south of a belt of westerlies in the center of the channel. (figure 33). The values of  $c_1$  as a function of the zonal wavelength in the series of computations are shown in figures 13,





14, and 15, corresponding to  $b = 1000, 4000$  and  $6000$  km, respectively.

It is seen that  $\beta$  and  $q$  have a stabilizing influence as in example 1, but an unstable band of wavelengths does exist for the case  $\beta = \beta_{45}$  and  $q^2 = 1.5 \times 10^{-12} \text{ m}^{-2}$ , even for  $b = 6000$  km. The maximum values of  $c_1$  (for  $\beta = q = 0$ ) occur nearly at  $\frac{L}{b} = 1.0$  and are greater than for any of the profiles previously discussed. However, the band of wavelengths in the case of

$\beta = q = 0$ , for which instability occurs, is much narrower than the others.

It may be concluded that this profile in the divergent model is more unstable than the single-jet profile in example 1.

Part II.  $N = 7$ , (or  $n = \frac{D}{8}$ ).

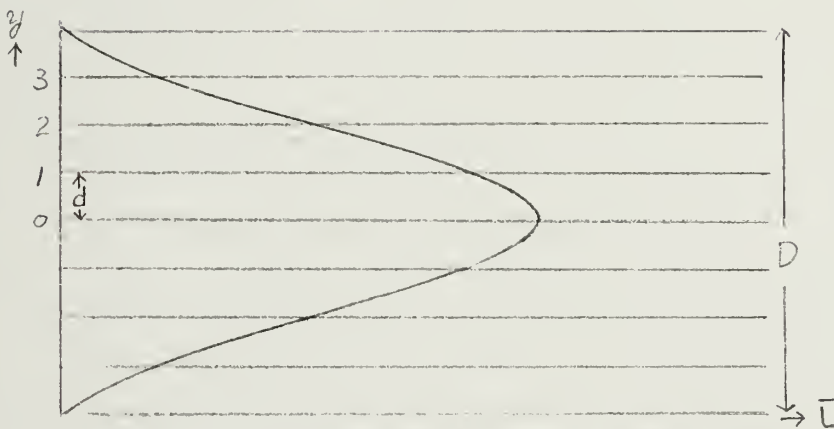


Fig. 16. The total wind channel showing the eight subdivisions.

The general validity of the conclusions which have been reached in preceding parts may be questioned because of the finite-difference mesh-size corresponding to  $N = 5$ .

As a check on the previous results, it will be of interest to study the case,  $N = 7$ , as depicted in figure 16. In this case the frequency equation (2.12) is replaced by a fourth-degree



equation of the form

$$C^4[hS_0 - T_0] + C^3[(hS_1 + G_0S_0) + 2V_0] + C^2[hS_2 + G_0S_1 + 2V_1] + C[hS_3 + G_0S_2 + 2V_2] + [G_0S_3 - 2V_3] = 0 \quad (2.18)$$

The notations in (2.18) have the following definitions:

$$P_n = d^2(\beta - \overline{U}_n) \quad ,$$

$$G_n = P_n - \overline{U}_n \gamma \quad , \quad (n = 0, 1, 2, 3.)$$

$$\gamma = 2 + u^2 d^2 \quad ,$$

$$h = \gamma + d^2 q^2 \quad ,$$

$$T_0 = h^2 - 1 \quad ,$$

$$T_1 = h(G_3 + G_2) + (\overline{U}_2 + \overline{U}_3) \quad ,$$

$$T_2 = G_2 G_3 - \overline{U}_2 \overline{U}_3 \quad ,$$

$$S_0 = h(T_0 - 1) \quad ,$$

$$S_1 = h(T_1 + \overline{U}_1 + \overline{U}_2) + G_1 T_0 - G_3 \quad ,$$

$$S_2 = h(T_2 - \overline{U}_1 \overline{U}_2) + G_1 T_1 + G_3(\overline{U}_1 + \overline{U}_2) \quad ,$$

$$S_3 = G_1 T_2 - G_3 \overline{U}_1 \overline{U}_2 \quad ,$$

$$V_0 = T_0(\overline{U}_0 + \overline{U}_1) - T_1 \quad ,$$

$$V_1 = T_1(\overline{U}_0 + \overline{U}_1) - \overline{U}_0 \overline{U}_1 T_0 - T_2 \quad ,$$

$$V_2 = T_2(\overline{U}_0 + \overline{U}_1) - \overline{U}_0 \overline{U}_1 T_1 \quad , \quad \text{and}$$

$$V_3 = \overline{U}_0 \overline{U}_1 T_2 \quad .$$



Solutions of equation (2.13) have been obtained by the Muller method [6] for the same series of examples as for the case,  $N = 5$ .

Since there exist differences in the instability characteristics of single-jet and double-jet profiles, it is of special interest to examine these cases using the finer mesh-size corresponding to  $N = 7$ .

Example 1. Single-jet basic current (fig. 2, curve (1)),

$$\bar{U} = B \left( 1 - \cos \frac{2\pi}{D} y \right) \quad (\text{Same as (2.13)}).$$

The values of  $c_1$  as a function of wavelength in the various series of computations are shown in figures 17, 18, and 19, corresponding to  $D = 2000, 4000$ , and  $6000$  km, respectively. A comparison to figures 3, 5, and 6 shows the two cases,  $N = 5$  and  $N = 7$ , to be very similar. However, some differences do exist for  $N = 7$  as follows:

- a)  $\beta$  has a destabilizing influence for relatively shorter wavelengths;
- b) the band of unstable wavelengths is slightly wider;
- c) the maximum values of  $c_1$  for  $\beta = q = 0$  occurs at  $\frac{L}{D} \approx 2.5$  instead of at 2.0;
- d) due to the lesser stabilizing effects of  $\beta$  and  $q$  with increasing meridional width,  $D$ , the unstable curve (5) in figure 18 for  $D = 4000$  km and curves (2) and (3) for  $D = 6000$  km have appeared (figure 19).

Example 2. Double-jet basic current (fig. 2, curve (2)),

$$\bar{U} = B \left( \sin \frac{\pi}{D} y + \sin \frac{3\pi}{D} y \right) \quad (\text{Same as (2.16)}).$$



As indicated, earlier greater differences might well have been expected in this case because the greater complexity of the double-jet profile is not as well represented by the subdivision into 6 parts ( $N = 5$ ).

The results for  $N = 7$  in this profile, shown in figures 20 and 21, are also quite similar to those for  $N = 5$  (figures 11 and 12) except as follows:

- 1) when  $D = 2000$  km;
  - a) the magnitude of  $c_i$  is nearly double;
  - b) since the destabilizing influences of  $\beta$  and  $q$  are much greater, the band of unstable wavelengths has widened;
- 2) when  $D = 4000$  km;
  - a) the maximum value of  $c_i$  for  $\beta = q = 0$  occurs at  $\frac{L}{D} \approx 1.5$ ;
  - b) the last three curves (3, 4 and 5) of figure 21 now show a stabilizing effect with increasing  $q$  for wavelengths given in this figure, but it seems probable that the effect of  $q$  will be reversed for sufficiently longer wavelengths;
  - c) for  $\beta = \beta_{45}$  and  $q^2 = 1.5 \times 10^{-12} \text{ m}^{-2}$ ,  $c_i$  vanishes at  $L = 5000$  km.

In summary, it may be stated that the essential features of the stability characteristics are similar for the cases  $N = 5$  and 7; however some details appear to be lost in the cruder subdivision of the basic channel corresponding to the case,  $N = 5$ .





### C. Fourier-series method.

If a series of trigonometric terms is used to represent  $\bar{U}(y)$  it appears appropriate to seek a solution of (2.6) for  $\phi(y)$  as a finite Fourier series of the form

$$\phi(y) = \sum_{n=1}^N \phi_n \sin(n\lambda y), \quad n = 1, 3, 5, \dots, N \quad (2.19)$$

where  $\lambda = \frac{\pi}{D}$ .

Then the expression (2.19) obviously satisfies the boundary conditions at the rigid walls at  $y = 0$  and at  $y = D$ .

As the value of  $N$  in (2.19) increases, more reliable results regarding the stability features may be expected. With-Nielsen [3] has found the stability characteristics for values of  $n$  up to 3.

Larger values of  $N$  (up to  $n = 8$ ) have been considered by Eliassen [2] but mostly in cases where the effects of  $\beta$  and divergence terms were excluded by assumption. His results showed the existence of only one unstable mode corresponding to odd values of  $n$ , and also that  $c_1$  at  $\frac{L}{D} = 2.0$  is the same for  $3 \leq n \leq 6$ , but somewhat smaller for  $n = 7$  and 8. Hence this study will be concerned only with small and odd values of  $n$ .

To verify further the results in the foregoing section, the symmetric, harmonic zonal velocity profiles will again be considered.

#### 1). Single-jet basic current:

$$\bar{U} = B \left( 1 - \cos \frac{2\pi y}{D} \right) \quad (\text{same as (1.13)}) \quad (2.20)$$

where  $B = 30 \text{ m sec.}^{-1}$

Considering the case  $N = 5$ , inserting (2.20) and (2.19) into (2.6) yields a system of linear homogeneous equations



$$[(\lambda^2 + \mu^2 + q^2)C + \beta - \frac{B}{2}(3\mu^2 - \lambda^2)]\phi_1 + [\frac{B}{2}(5\lambda^2 + \mu^2)]\phi_3 = 0$$

$$[\frac{B}{2}(\mu^2 - 3\lambda^2)]\phi_1 + [(9\lambda^2 + \mu^2 + q^2)C + \beta - B(9\lambda^2 + \mu^2)]\phi_3 + [\frac{B}{2}(21\lambda^2 + \mu^2)]\phi_5 = 0 \quad (2.21)$$

$$[\frac{B}{2}(5\lambda^2 + \mu^2)]\phi_3 + [(25\lambda^2 + \mu^2 + q^2)C + \beta - B(25\lambda^2 + \mu^2)]\phi_5 = 0$$

In order to have non-trivial solutions for  $\phi_1$ ,  $\phi_3$ , and  $\phi_5$ , the determinant must vanish, which gives the frequency equation

$$C^3(RWE) + C^2[E(RV+SW) + RWG] + C[E(SV-TH) + G(RV+SW) - PHW] + [G(SV-TH) - PHV] = 0 \quad (2.22)$$

where  $E = \lambda^2 + \mu^2 + q^2$ ,  $G = \beta - \frac{B}{2}(3\mu^2 - \lambda^2)$ ,

$$H = \frac{B}{2}(5\lambda^2 + \mu^2), \quad P = \frac{B}{2}(\mu^2 - 3\lambda^2),$$

$$R = 9\lambda^2 + \mu^2 + q^2, \quad S = \beta - B(9\lambda^2 + \mu^2),$$

$$T = \frac{B}{2}(21\lambda^2 + \mu^2), \quad W = 25\lambda^2 + \mu^2 + q^2,$$

and  $V = \beta - B(25\lambda^2 + \mu^2)$ .

In the case,  $N = 7$ , the frequency equation (2.22) is replaced by the fourth-degree equation:

$$C^4(YRWE) + C^3(YK_0 + ZRWE) + C^2(YK_1 + ZK_0 - TREX) + C[YK_2 + ZK_1 - (ES + RG)TX] + [ZK_2 - (GS - PH)TX] = 0 \quad (2.23)$$

where  $X = \frac{B}{2}(\mu^2 + 45\lambda^2)$ ,  $Y = 49\lambda^2 + \mu^2 + q^2$ ,

$$Z = \beta - B(49\lambda^2 + \mu^2), \quad M_0 = RV + SW,$$

$$M_1 = SV - TH, \quad K_0 = EM_0 + RWG,$$

$$K_1 = EM_1 + GM_0 - PHW,$$

and  $K_2 = GM_1 - PHV$ .



The roots of (2.22) and (2.23) for the previous series of computations are shown in figures 22, 23, 24, 25, 26, and 27, corresponding to  $\beta = 2000$ , 4000, and 6000 for the cases,  $N = 5$ , and  $N = 7$ .

There is obviously a close similarity in the essential features of the stability characteristics among the cases,  $N = 3$  (given in Wiin-Nielsen [5]),  $N = 5$  and  $N = 7$ . Furthermore, there also exist similarities between the results of the finite-difference method and those of the Fourier-series method. It may be noted that the results of the case,  $\beta = \frac{D}{C}$  ( $N = 5$ ), in the former method are particularly close to the results of the case  $N = 3$  in the Fourier-series method, while the results of the case,  $\beta = \frac{D}{C}$  ( $N = 7$ ), correspond more nearly to those for  $N = 5$ .

It may be concluded that the results for small values of  $N$  generally represent the essential features of the stability characteristics in the quasi-barotropic flow; however the following differences with increasing  $N$  do appear:

- a) the maximum value of  $c_i$  for  $\beta = q = 0$  is less ( $c_{i \text{ max.}} = 9.57 \text{ m sec}^{-1}$  for  $N = 5$  and  $8.40 \text{ m sec}^{-1}$  for  $N = 7$ );
- b) the stabilizing effects of  $\beta$  and  $q$  with increasing  $N$  are less pronounced;
- c) the maximum values of  $c_i$  are shifted toward longer wavelengths such that for the case  $\beta = 0$  and  $q = 0$  they occur at  $\frac{L}{D} = 2.0$ , for  $N = 3$ ;  $\frac{L}{D} = 2.5$ , for  $N = 5$ ;



and  $\frac{L}{D} = 3.0$ , for  $R = 1$ ;

c) the pairs of local wavelengths for which instability occurs become larger.

2). Double-jet basic current:

$$\bar{U} = B \left( 1 - \cos \frac{4\pi}{D} y \right) \quad (2.24)$$

where  $B = 30 \text{ m sec}^{-1}$ .

This profile has  $\bar{U} = 0$  at both rigid walls and at the center of the channel, and also has  $\bar{U} = 2B$  at  $y = \frac{D}{4}$  and at  $y = \frac{3}{4} D$  (fig. 34,  $\bar{U} = (0)$ ).

By inserting (2.24) and (2.19) ( $N = 1$ ) into (2.6), the following set of linear homogeneous equations is obtained:

$$\begin{aligned} &[(\lambda^2 + \mu^2 + q^2)C + \beta - B(\lambda^2 + \mu^2)]\phi_1 + \left[\frac{B}{2}(7\lambda^2 - \mu^2)\right]\phi_3 + \left[\frac{B}{2}(9\lambda^2 + \mu^2)\right]\phi_5 = 0 \\ &\left[\frac{B}{2}(15\lambda^2 - \mu^2)\right]\phi_1 + [(9\lambda^2 + \mu^2 + q^2)C + \beta - B(9\lambda^2 + \mu^2)]\phi_3 = 0 \quad (2.25) \\ &\left[\frac{B}{2}(\mu^2 - 15\lambda^2)\right]\phi_1 + [(25\lambda^2 + \mu^2 + q^2)C + \beta - B(25\lambda^2 + \mu^2)]\phi_5 = 0. \end{aligned}$$

In order to have non-zero solutions for  $\phi_1$ ,  $\phi_3$  and  $\phi_5$ , the determinant must vanish. This condition gives the frequency equation

$$\begin{aligned} &C^3(WEK) + C^2[W(ES+RG) + V'ER] + C[P'TR + W(GS+PH) \\ &+ V(ES+RG)] + [P'TS + V(GS+PH)] = 0 \end{aligned} \quad (2.26)$$

where  $E = \lambda^2 + \mu^2 + q^2$ ,  $G = \beta - B(\lambda^2 + \mu^2)$ ,

$H = \frac{B}{2}(7\lambda^2 - \mu^2)$ ,  $T = \frac{B}{2}(9\lambda^2 + \mu^2)$ ,

$S = \frac{B}{2}(15\lambda^2 - \mu^2)$ ,  $R = 9\lambda^2 + \mu^2 + q^2$ ,

$S = \beta - B(9\lambda^2 + \mu^2)$ ,  $W = 25\lambda^2 + \mu^2 + q^2$ ,

and  $V = \beta - B(25\lambda^2 + \mu^2)$ .





This frequency equation (2.10) has been solved numerically for the previous series of computations. The values of  $c_1$  with respect to wavelength are shown in figures 28, 29 and 30.

It is seen that  $\beta$  and  $q$  effects do not give a stabilizing influence for all wavelengths. For relatively longer wavelengths,  $\beta$  and  $q$  have a destabilizing influence on the perturbations in the sense that the band of unstable wavelengths is much broader than in the case  $\beta = 0$  or  $q = 0$ . Moreover, the waves are more unstable with increasing meridional width  $D$ . Hence the divergent, one-parameter model in this double-jet wind profile is more unstable than the non-divergent model. These results are consistent with those in the previous example for a double-jet profile in which the method of finite differences has been used.

For this profile, if even values of  $n$  ( $n = 2, 4, 6$ ) in (2.19) are included, there exists other amplifying modes different from those previously discussed, which are not shown in this paper.



### 3. Stability properties of the stratified model.

The vorticity equation for this model has been obtained by Arnason [8] and may be written in the form

$$(\nabla^2 - q^2) \frac{\partial \psi}{\partial t} + \mathbf{V} \cdot \nabla (\nabla^2 \psi + f) - q^2 \nabla \cdot \nabla \psi = 0 \quad (3.1)$$

where  $q^2 = \frac{f(\nabla^2 \psi + f)}{g'' H}$ ,  $\mathbf{V} = \mathbf{k} \times \nabla \psi$ , and  $\nabla = \bar{U} \mathbf{i}$ . Here  $H$  is the thickness of the stratified layer, and  $g''$  is the acceleration of gravity corrected for compressibility.

By using the perturbation method, (3.1) can be reduced to the form

$$(\nabla^2 - q^2) \frac{\partial \psi'}{\partial t} + \bar{U} \frac{\partial}{\partial x} (\nabla^2 \psi') + \frac{\partial \psi'}{\partial x} \left( \beta - \frac{d^2 \bar{U}}{dy^2} - q^2 \bar{U} \right) = 0 \quad (3.2)$$

where  $\psi'$  is the perturbation stream function and  $\bar{U} = \bar{U}(y)$  is the mean zonal velocity.

Substituting  $\psi'(x, y, t) = \phi(y) e^{i\mu(x - ct)}$  into (3.2) yields

$$(\bar{U} - c)(\phi'' - \mu^2 \phi) + [\beta - \bar{U}'' + q^2(\bar{U} - c)] \phi = 0 \quad (3.3)$$

where the primes denote differentiation with respect to  $y$ .

In comparison with (2.6), equation (3.3) has one more term which is peculiar to this model. Thus it may be expected that the stability characteristics in this model will differ somewhat from those of the previous divergent, one-parameter model.

The analysis will be restricted to the initial zonal wind profile of the type

$$\bar{U} = B \left( 1 - \cos \frac{2\pi}{D} y \right) \quad (\text{same as (2.13)}),$$



and also to the case  $D = 0$  in the Appendix (3.25). The resulting frequency equation is

$$C^2(RUE) + C^2[E(RV+SW) + KU] + C[E(SV-TH) + G(RV+SW) - PHU] + [G(SV-TH) - THV] = 0 \quad (3.4)$$

$$\text{where } E = \lambda^2 + u^2 + q^2, \quad G = \beta - \frac{B}{2}(3u^2 + 3q^2 - \lambda^2),$$

$$H = \frac{B}{2}(5\lambda^2 + u^2 + q^2), \quad P = \frac{E}{2}(u^2 + q^2 - 3\lambda^2),$$

$$R = 9\lambda^2 + u^2 + q^2, \quad S = \beta - B(9\lambda^2 + u^2 + q^2),$$

$$T = \frac{E}{2}(21\lambda^2 + u^2 + q^2), \quad W = 21\lambda^2 + u^2 + q^2,$$

$$\text{and } V = \beta - B(25\lambda^2 + u^2 + q^2).$$

The results of the previous computation series are given in figures 31 and 32, corresponding to  $D = 2000$  and  $4000$  km.

It is seen by comparing the curves (2) and (3) in figure 31 that  $q$  has a destabilizing influence for relatively longer wavelengths (longer than the wavelength at which the maximum  $c_i$  for curve (2) occurs). Moreover, these effects are verified with increasing values of  $q$ , as given by curves (4) and (5). Hence the divergent, stratified model is more unstable than the non-divergent one. Also comparison of figures 31 and 22 shows that the stratified model is more unstable than the previous one-parameter model.

These results are also verified by figure 32, which contains similar results for  $D = 4000$  km. Note that the waves are more stable with increasing  $D$ . Nevertheless, for the case  $\beta = \beta_{45}$ ,  $q^2 = 1.5 \times 10^{-12} \text{ m}^{-2}$  and  $D = 4000$  km, it seems possible to have



a ,and of unstable waves at longer wavelengths which are not shown  
in this figure.





#### 4. Momentum changes.

It is of special interest to see what may be inferred from the solutions of this particular problem about the effects of the unstable perturbations on the basic flow through momentum transfer. Changes in the zonal current would alter the profile so radically that the initial solution of the perturbation problem no longer applies. This implies that the basic profile may, in turn, alter the structure of the perturbations.

Recently in the paper by Niin-Nielsen [3], it has been found that a single-jet zonal wind profile initially can change to a double-jet profile in one or two days due to meridional momentum transport by the eddies.

It is obviously of interest to determine how an initial double-jet wind profile will change as a result of momentum transport by the unstable perturbations.

In this section, we will consider the double-jet basic current

$$\bar{U} = B \left( 1 - \cos \frac{4\pi}{D} y \right) \quad (\text{same as (2.24)}),$$

which is designated by  $\bar{U}(0)$  in figure 3a.

From the equation of motion, the changes in the mean zonal current can be expressed in the form

$$\frac{\partial \bar{U}}{\partial t} = - \frac{\partial \overline{u'v'}}{\partial y} \quad (4.1)$$

where the prime designates the perturbations and the bar refers to the zonal mean

$$\bar{U} = \frac{1}{L} \int_0^L U \, dx.$$



Thus the perturbation of the magnetic field profile can be computed from the distributional convergence of the long-wavelength transport.

In order to evaluate this quantity, from the solution of the perturbation problem, equation (4.1) may be written in the form

$$\frac{\partial \Psi}{\partial t} = 2 \mu \chi^2 [e^{2 \mu C_1 t} (\phi_1 \ell_2 - \phi_2 \ell_1) + e^{-2 \mu C_2 t} (\phi_1 m_2 - \phi_2 m_1) + (\eta_1 \phi_2 - \eta_2 \phi_1 + \ell_1 \ell_2 - \ell_2 \ell_1)] \cdot M(\beta) \quad (4.2)$$

The notation have the following definitions:

$$C_1 = C_r + i C_i, \quad C_2 = C_r - i C_i,$$

$$M(\beta) = \cos \frac{4\pi}{D} \beta - \cos \frac{2\pi}{D} \beta, \quad (4.3)$$

$$\phi_1^{(1)} = \phi_1 + i \phi_2$$

$$\phi_1^{(2)} = \ell_1 + i \ell_2$$

$$\phi_2^{(1)} = \ell_1 + i \ell_2$$

$$\phi_2^{(2)} = \eta_1 + i \eta_2$$

Here the superscripts denote the amplitudes of the perturbations (the equation (2.13)) corresponding to the two roots of the frequency equation (a quadratic equation),  $c_1$  and  $c_2$ , respectively.

A derivation of this equation has been given by Witt-Nielsen

[1, pp. 465]. Moreover, equations (3.9) and (3.10) in his paper must be replaced by

$$F(\zeta) = \left(1 + \frac{\lambda^2}{\mu^2} + \frac{q^2}{\mu^2}\right) \zeta + \frac{B}{\mu^2} - b \left(1 + \frac{\lambda^2}{\mu^2}\right) \quad (4.4)$$

$$\text{and } G = \frac{B}{2} \left(7 \frac{\lambda^2}{\mu^2} - 1\right). \quad (4.5)$$







( $\eta = 0$ ), a calculated value of  $\beta = 3000$  for  $L = 4000$  corresponds to  $\beta = 2000$  in Figure 3. The phase velocity is calculated for the case  $\beta = 3$  in (3.12) at  $\eta = 0$  and  $L = 4000$  (see Figure 3). The value of 2000 is thus associated with the maximum instability when  $\beta = 3000$  m (in this case  $\beta = 16.9 \pm 1.12$  sec<sup>-1</sup>).

The amplitude  $A_1$  of the real component of the initial perturbation stream function is chosen to correspond to a meridional velocity  $u = 10$  sec<sup>-1</sup> ( $A_1 = 1.5 \times 10^9$  m<sup>2</sup> sec<sup>-1</sup>),  $A_2 = A_3 = 0$ , and  $\theta = 35^\circ$  in (3.11). In general,  $A_1$  and  $A_2$  are related to  $\beta$ 's as follows:

$$\begin{aligned} \Phi_1'' + \beta_1 \Phi_1 &= 0 \\ \Phi_2'' + \beta_2 \Phi_2 &= 0 \end{aligned}$$

After 2.5 days the initial profile has changed to the single jet profile.

Figure 3b would be compared with Figure 3a since the parameters have the same values except that  $A_2 = A_3 = 1.5 \times 10^9$  m<sup>2</sup> sec<sup>-1</sup>. Again a comparison of the two jet profiles will indicate the single jet profile has decreased, but at a slightly faster rate for  $A_2 \neq 0$  than in the case  $A_2 = 0$ .

Figure 3c contains the distribution of  $\bar{U}(y, t)$  as a function of time for  $\beta = 1600$  m,  $L = 4000$  m corresponding to maximum instability for  $\eta = 0$ , and same parameters as in Figure 3b. In this case the merging rate is much slower than the larger  $\beta$  and  $L$ . This also can be shown by examination of equation (4.0).

It is obvious from (4.0) that if the imaginary part of the phase velocity vanishes ( $\alpha_i = 0$ ), which means barotropic stability,





the zonal velocity is independent of time. Hence the changes predicted in the zonal profile from these computations are due to the presence of transient barotropic waves.

Thus it may be concluded that if there exists barotropic instability in a basic flow characterized by a double maximum, it is a dynamical consequence of the convergence of meridional transport of momentum by the eddies that the zonal current tends to develop a single maximum of zonal velocity. This results from momentum being concentrated in the center of the channel by the eddies at the expense of both maxima.



## 2. Summary.

In section 2 the stability of barotropic flow for the divergent, one-parameter model has been investigated for various symmetrical zonal wind fields, including single-jet and double-jet profiles. Two different approximations are used for the amplitude of the perturbation stream function, one of which is based on a method of finite differences, and the second on a representation by a finite Fourier series.

The basic equation in this study is the vorticity equation which, for a harmonic wave solution, reduces to a second-order differential equation with variable coefficients for the perturbation amplitude.

The main conclusions are that the two methods give essentially the same results. Secondly, the introduction of divergence into the model in the form of a Helmholtz term tends to reduce the instability present in the non-divergent model for a single-jet zonal wind profile, while the reverse holds for a double-jet profile. Thirdly, it is also found that the waves in the divergent model are more stable with increasing wavelength both between the asymmetric ridge boundaries for a single-jet profile, while the reverse again holds for a double-jet profile.

Section 3 is concerned with the stability characteristics of Arnason's "stratified" barotropic model using a finite Fourier series for the perturbation stream function. It was found that the divergent, stratified model is more unstable than the non-divergent one; and also even more unstable than the



divergent, one-parameter model.

In section 4 the second-order effects of the unstable perturbations on an initial double-jet zonal flow are investigated.

It was found that this type of profile of the zonal wind changes to a single-jet zonal flow in a few days, solely due to the convergence of meridional transport of momentum in the center of the channel caused by the unstable barotropic perturbations.



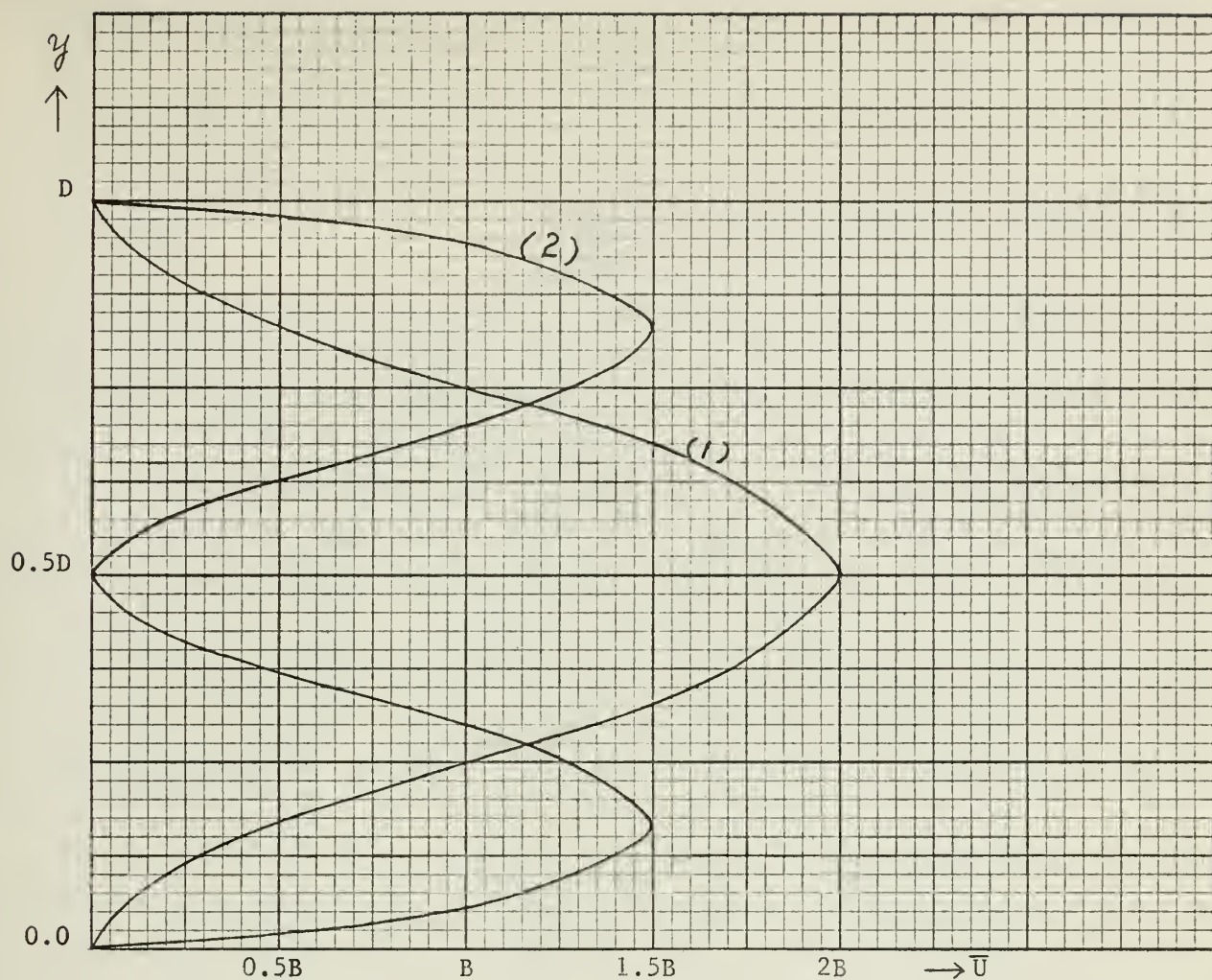


Fig. 2. The profiles of the zonal wind. Curve (1):  $\bar{U} = B(1 - \cos \frac{2\pi}{D}y)$ ;  
 (2):  $\bar{U} = B(\sin \frac{\pi}{D}y + \sin \frac{3\pi}{D}y)$ .





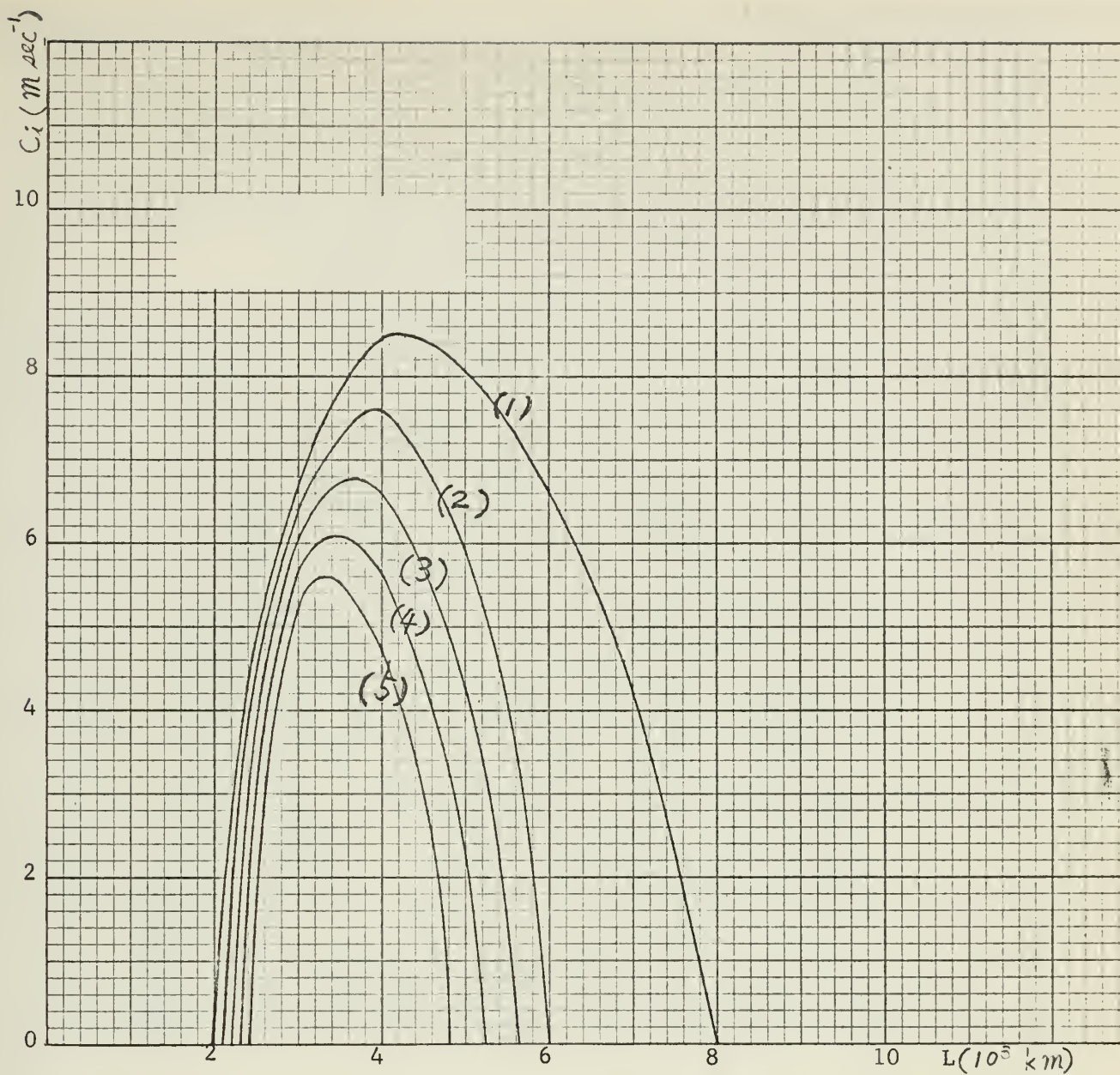


Fig. 3. The imaginary part,  $c_i$ , of the solution to equation (2.12) as a function of wavelength for  $\bar{U}=B(1-\cos(2\pi y/D))$ ,  $d = D/6$ ,  $D = 2000$  km, and  $B = 30$  m sec $^{-1}$ . Curve (1):  $\beta = 0$ ,  $q = 0$ ; (2):  $\beta = \beta_{45}$ ,  $q = 0$ ; (3):  $\beta = \beta_{45}$ ,  $q^2 = 0.5 \times 10^{-12}$  m $^{-2}$ ; (4):  $\beta = \beta_{45}$ ,  $q^2 = 1.0 \times 10^{-12}$  m $^{-2}$ ; (5):  $\beta = \beta_{45}$ ,  $q^2 = 1.5 \times 10^{-12}$  m $^{-2}$ .



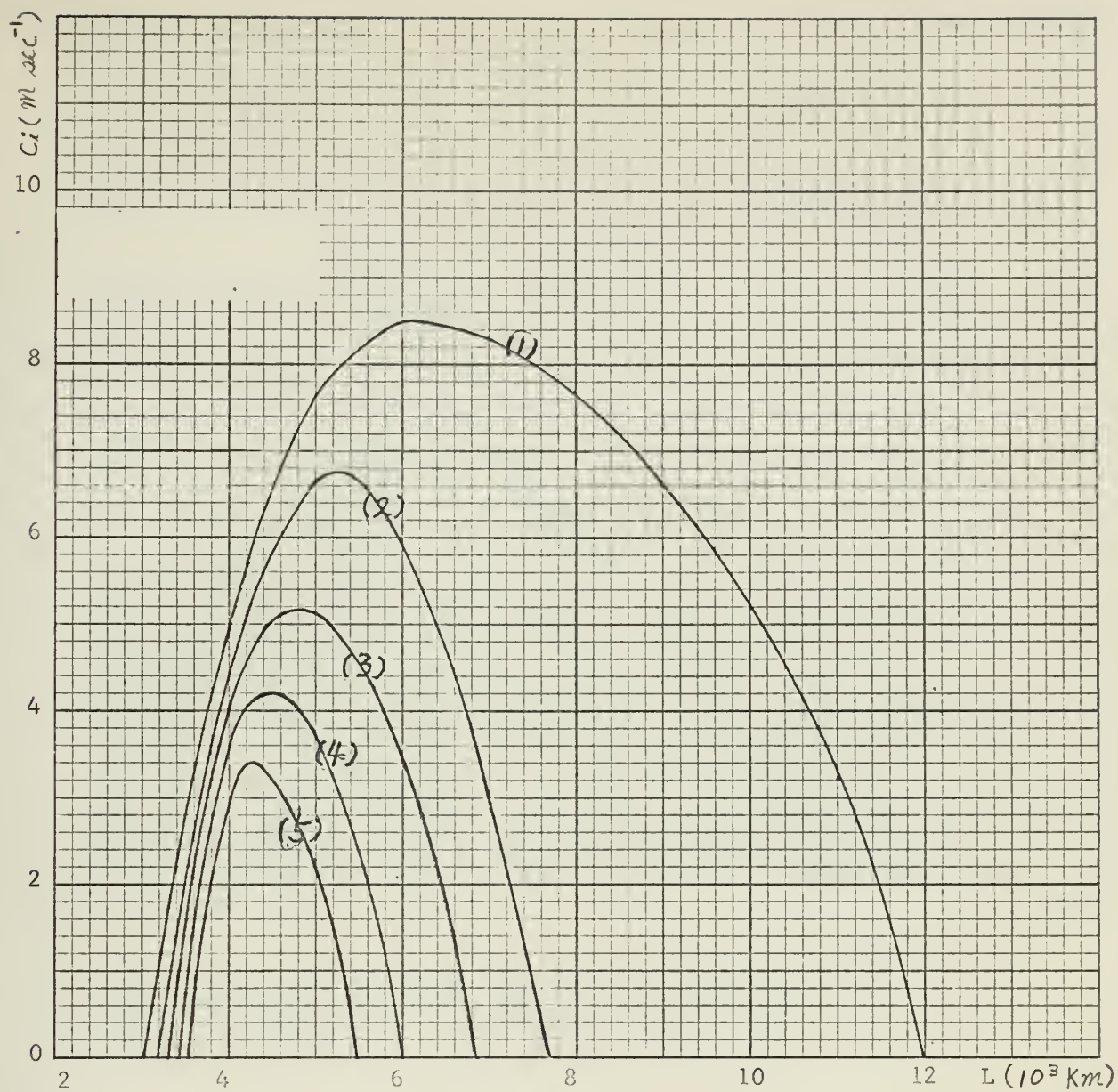


Fig. 4. The imaginary part,  $c_i$ , of the solution to equation (2.12) as a function of wavelength for the same parameters as in fig. 3 except  $D = 3000$  km. The curves as in fig. 3.



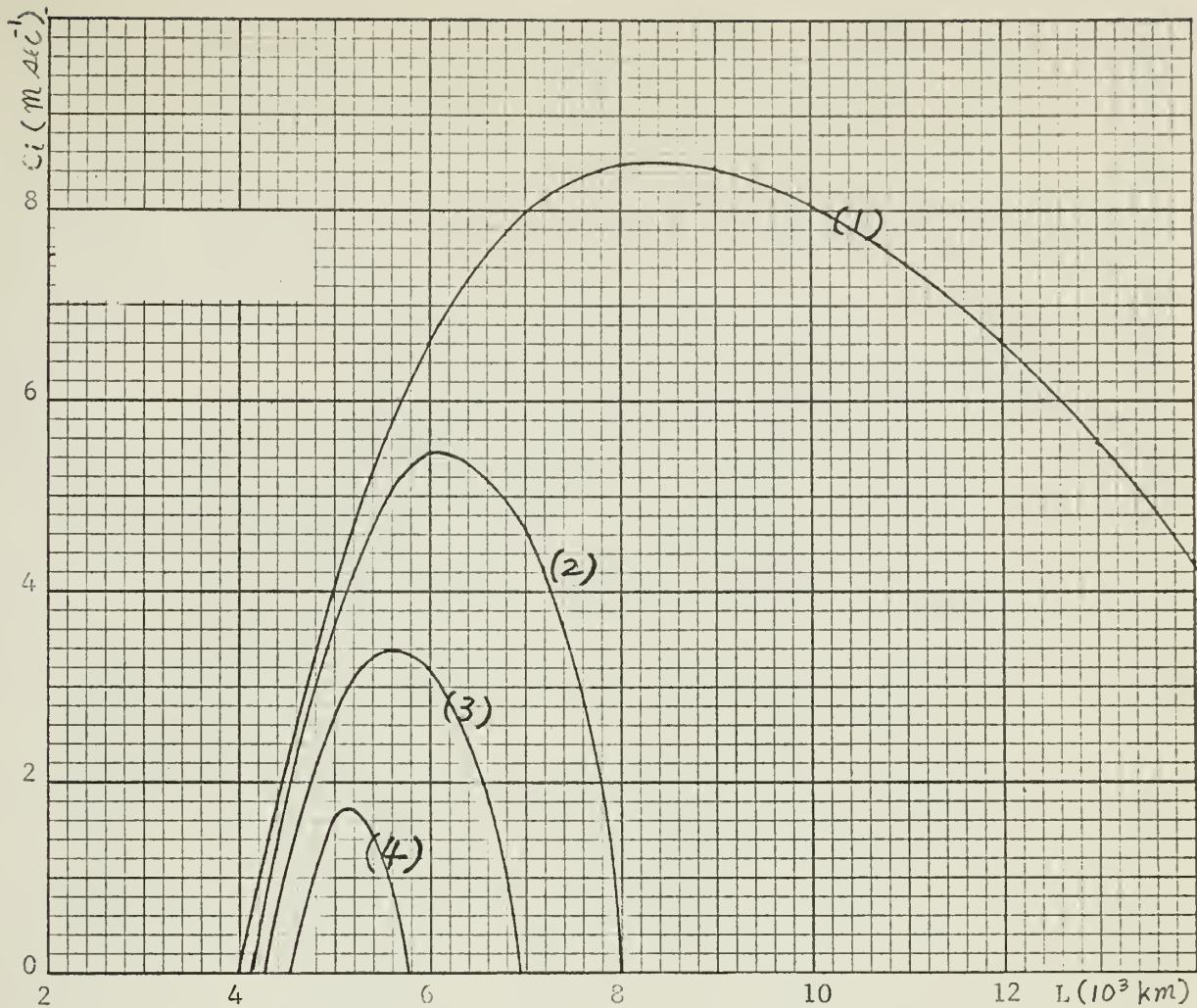


Fig. 5. The imaginary part,  $c_i$ , of the solution to equation (2.12) as a function of wavelength for the same parameters as in fig. 3 except  $D = 4000$  km. The curves as in fig. 3.





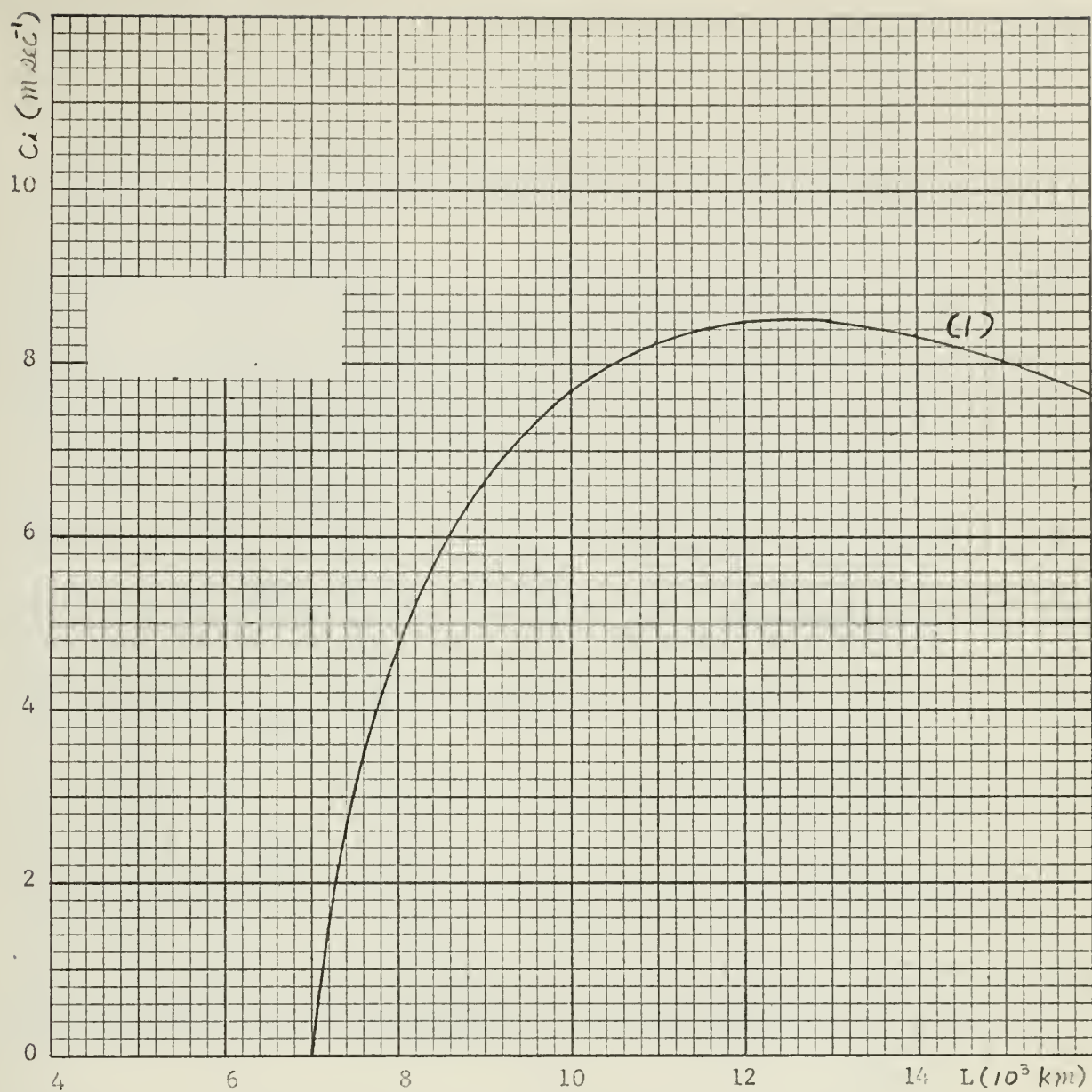


Fig. 6. The imaginary part,  $c_i$ , of the solution to equation (2.12) as a function of wavelength for the same parameters as in fig. 3 except  $D = 6000$  km. The curve (1) as in fig. 3.





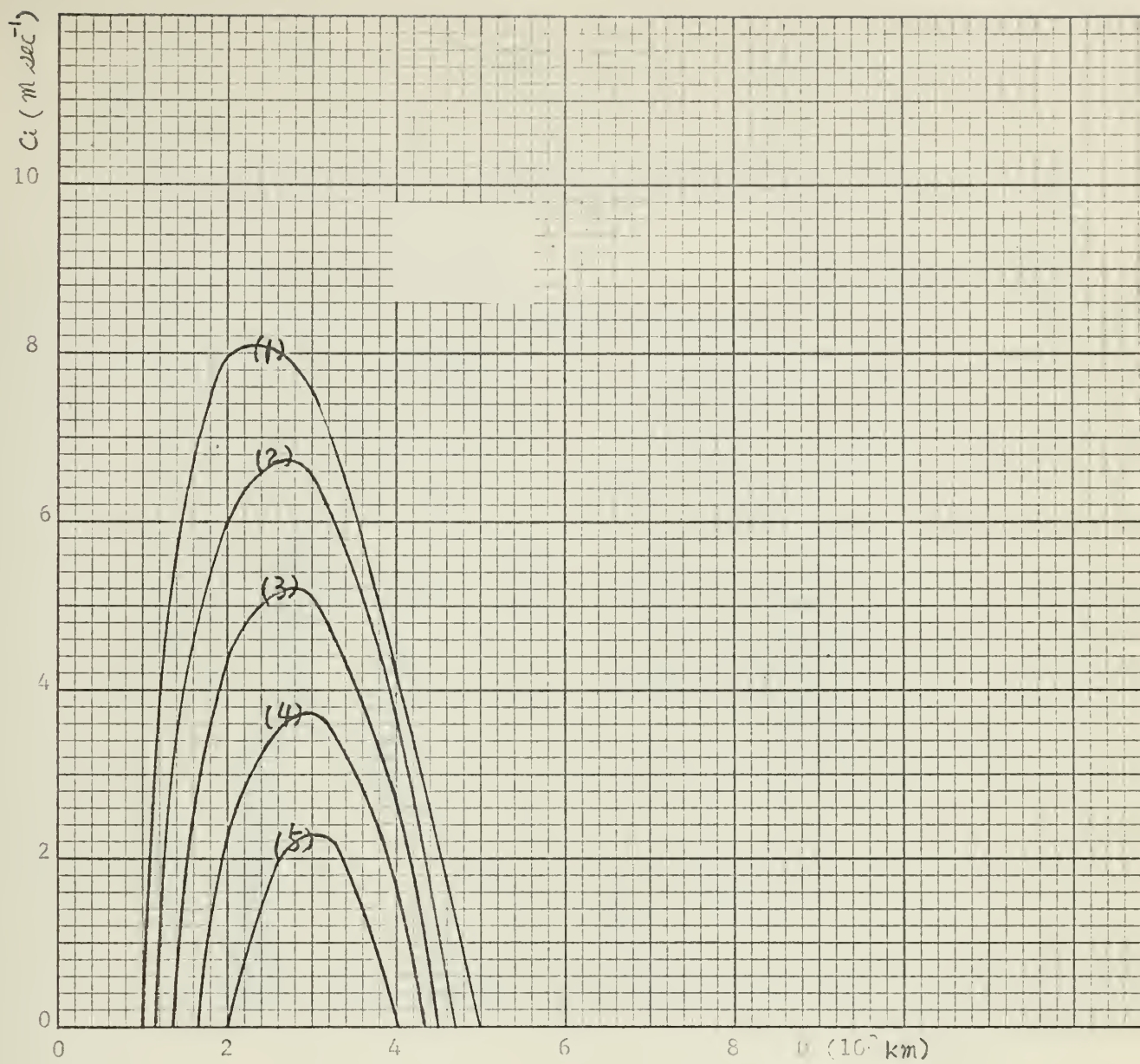


Fig. 7. The imaginary part,  $c_i$ , of the solution to equation (2.12) as a function of the meridional width  $D$  for  $L = 5000$  km and the same parameters as in fig. 3. The curves as in fig. 3.



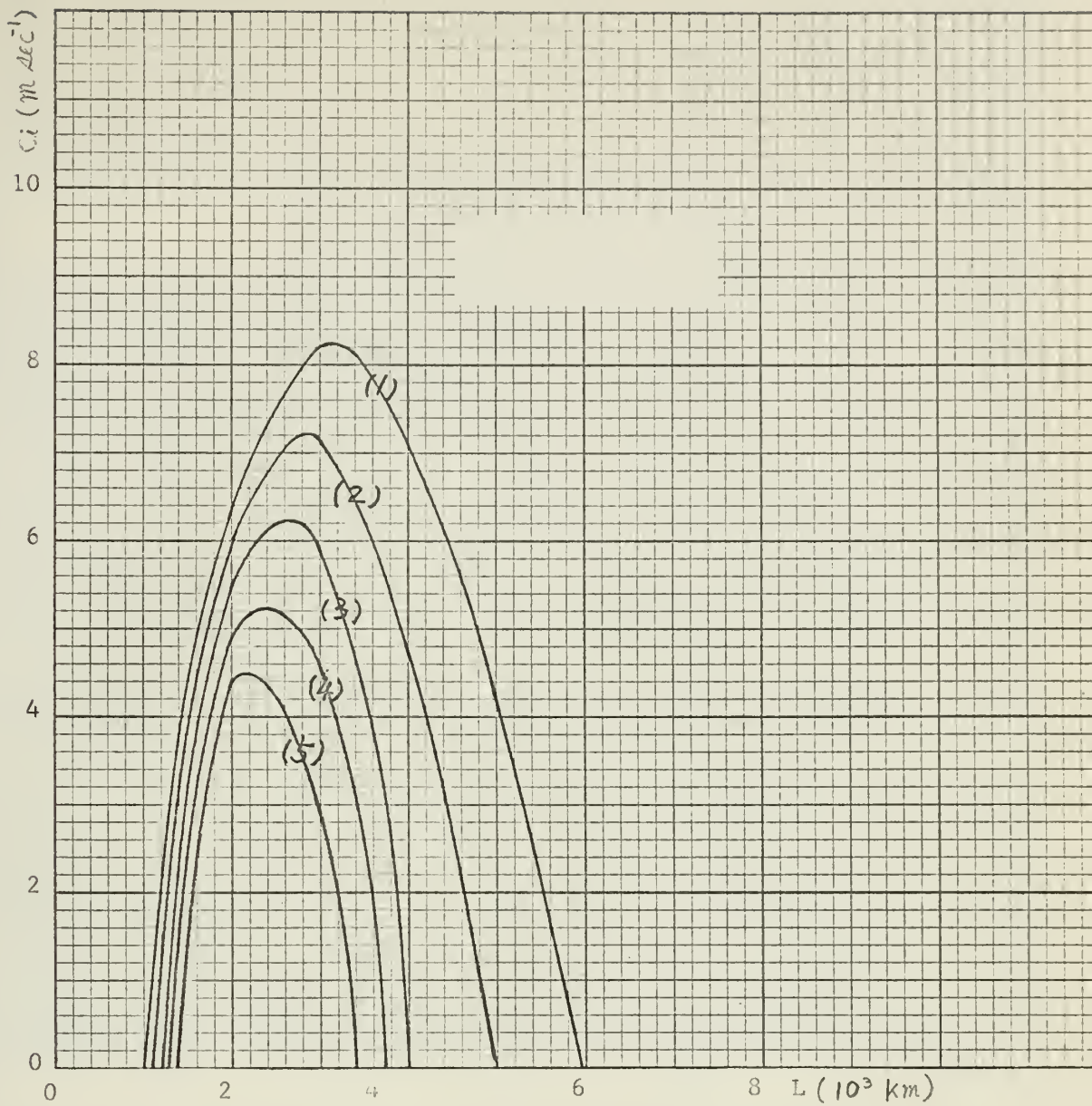


Fig. 8. The imaginary part,  $c_i$ , of the solution to equation (2.12) as a function of wavelength for  $U_0 = 2B$ ,  $U_1 = B$ ,  $U_2 = 0.5B$ ,  $d = D/6$ ,  $D = 2000$  km, and  $B = 30$  m sec<sup>-1</sup>. The curves (1), (2), (3), (4), and (5) as in fig. 3.



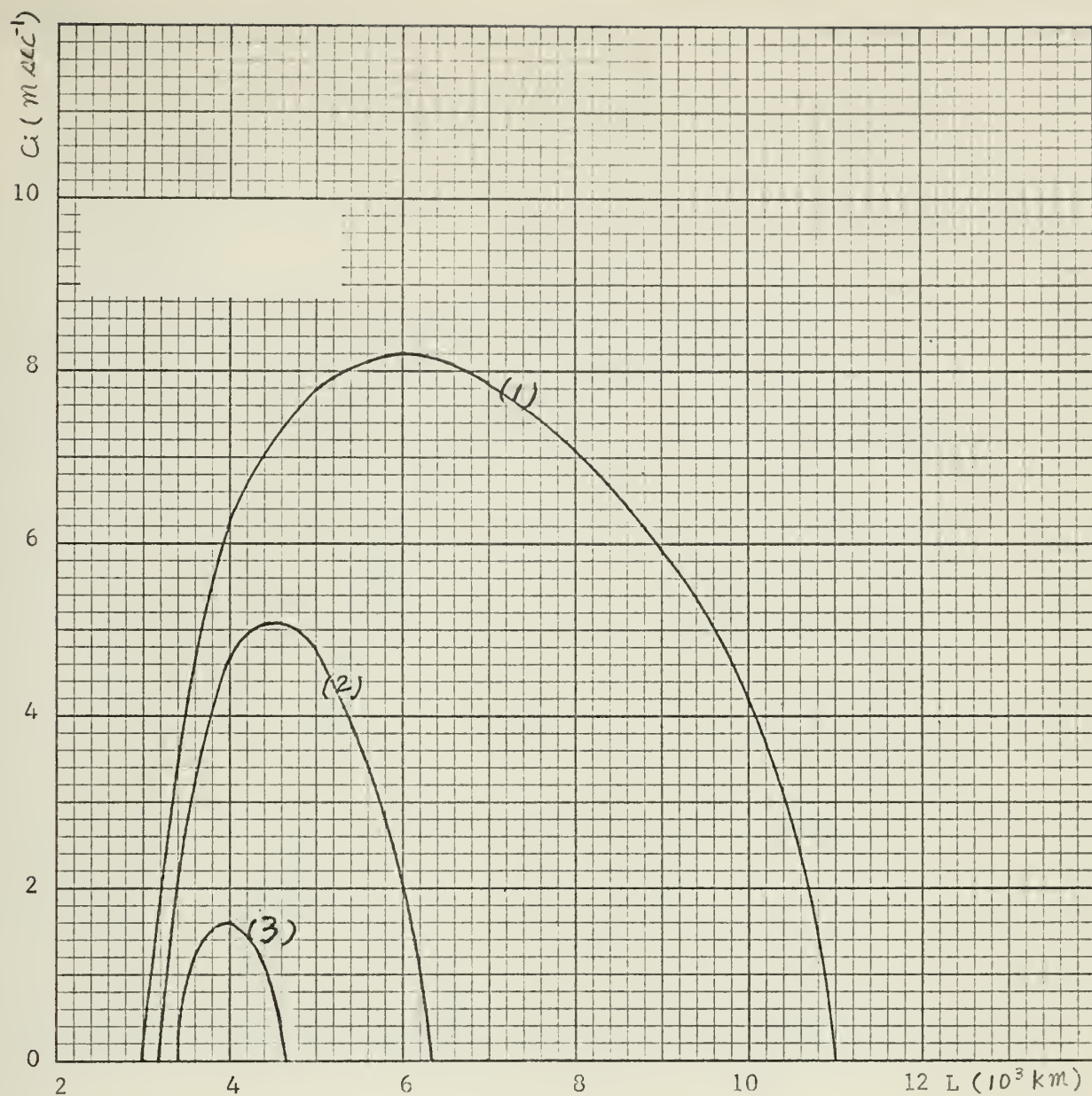


Fig. 9. The imaginary part,  $c_i$ , of the solution to equation (2.12) as a function of wavelength for the same parameters as in fig. 8 except  $D = 4000$  km. The curves as in fig. 3.





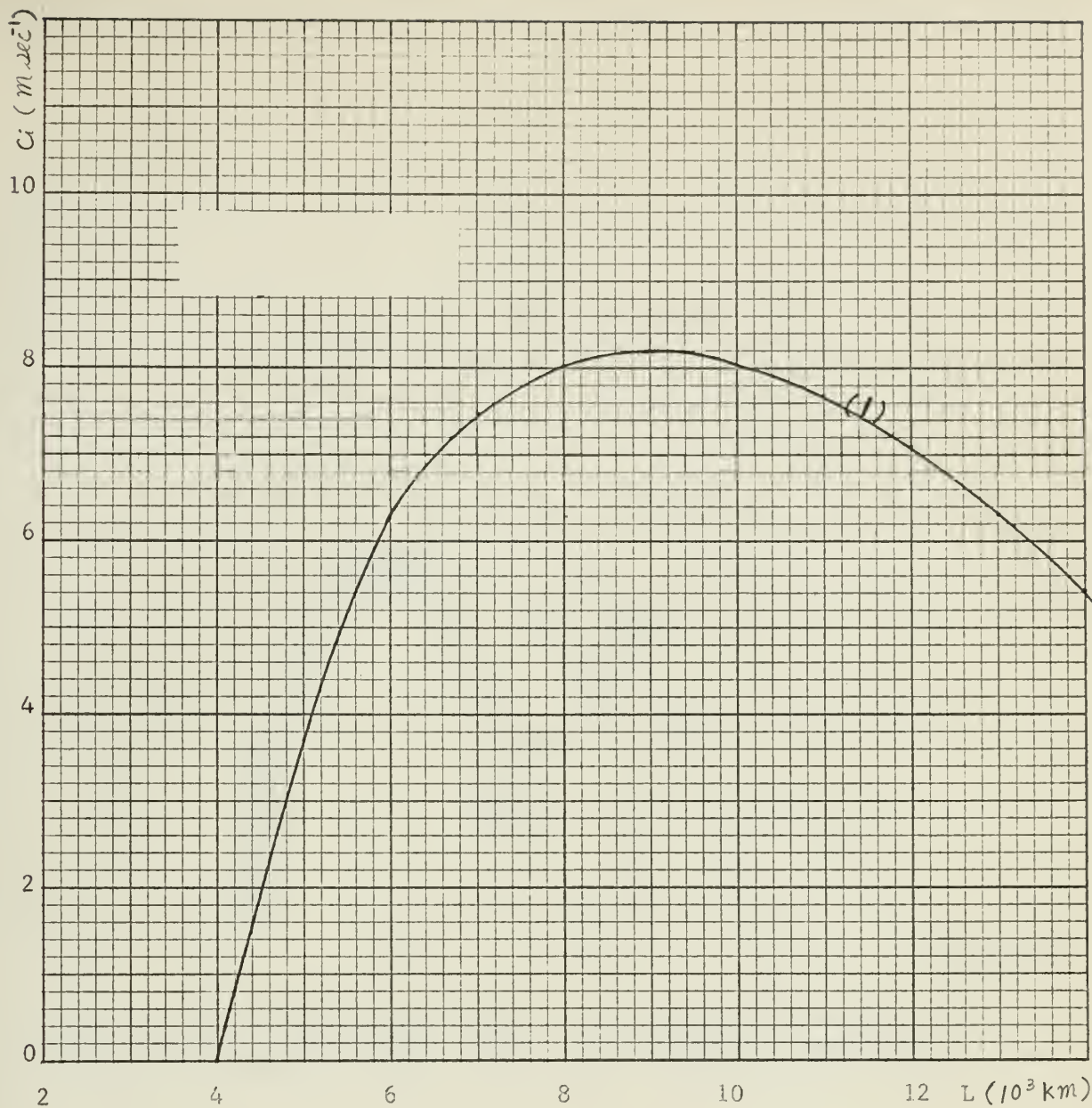


Fig. 10. The imaginary part,  $c_i$ , of the solution to equation (2.12) as a function of wavelength for the same parameters as in fig. 8 except  $D = 6000$  km. The curve (1) as in fig. 3.





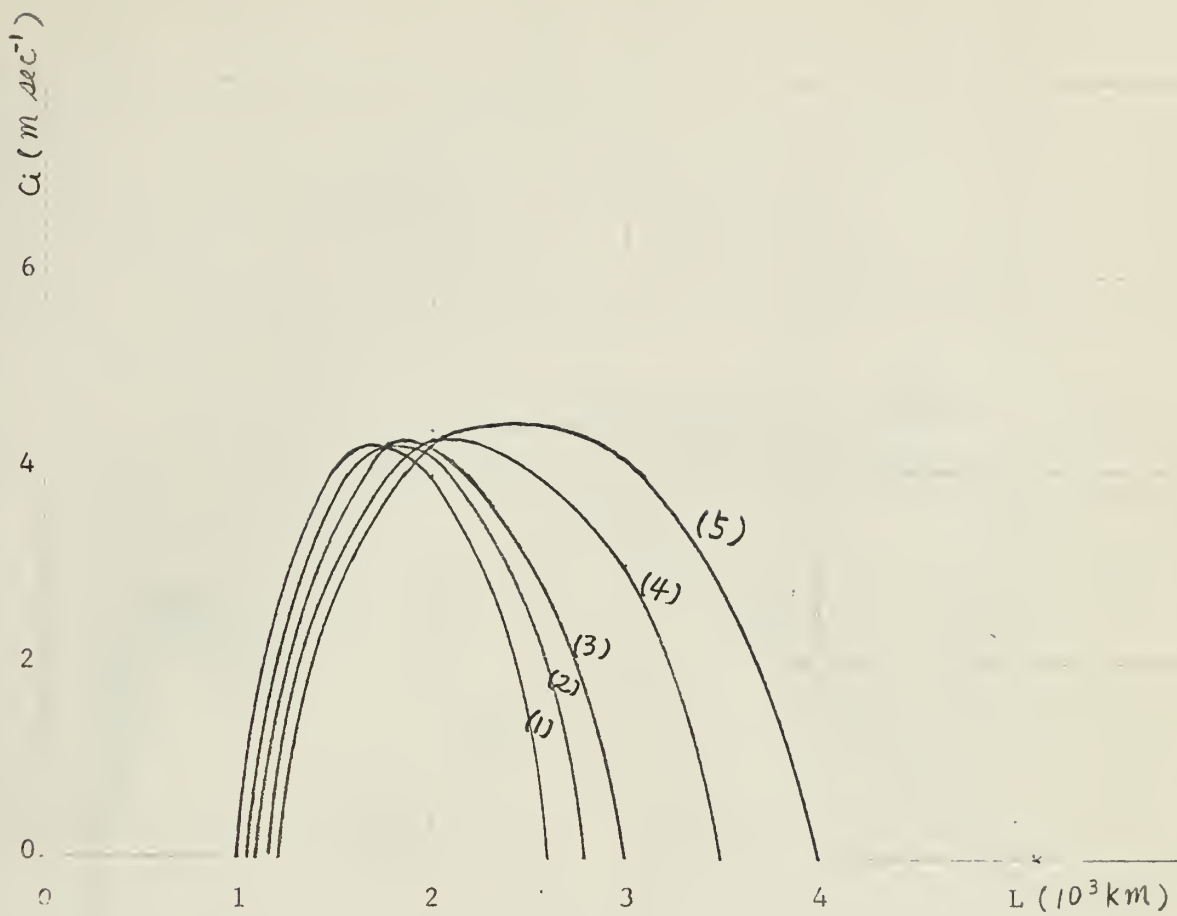


Fig. 11. The imaginary part,  $c_i$ , of the solution to equation (2.12) as a function of wavelength for  $U = B(\sin(\pi y/D) + \sin(3\pi y/D))$ ,  $d = D/6$ ,  $D = 2000$  km, and  $B = 40$  m sec $^{-1}$ . The curves as in fig. 3.



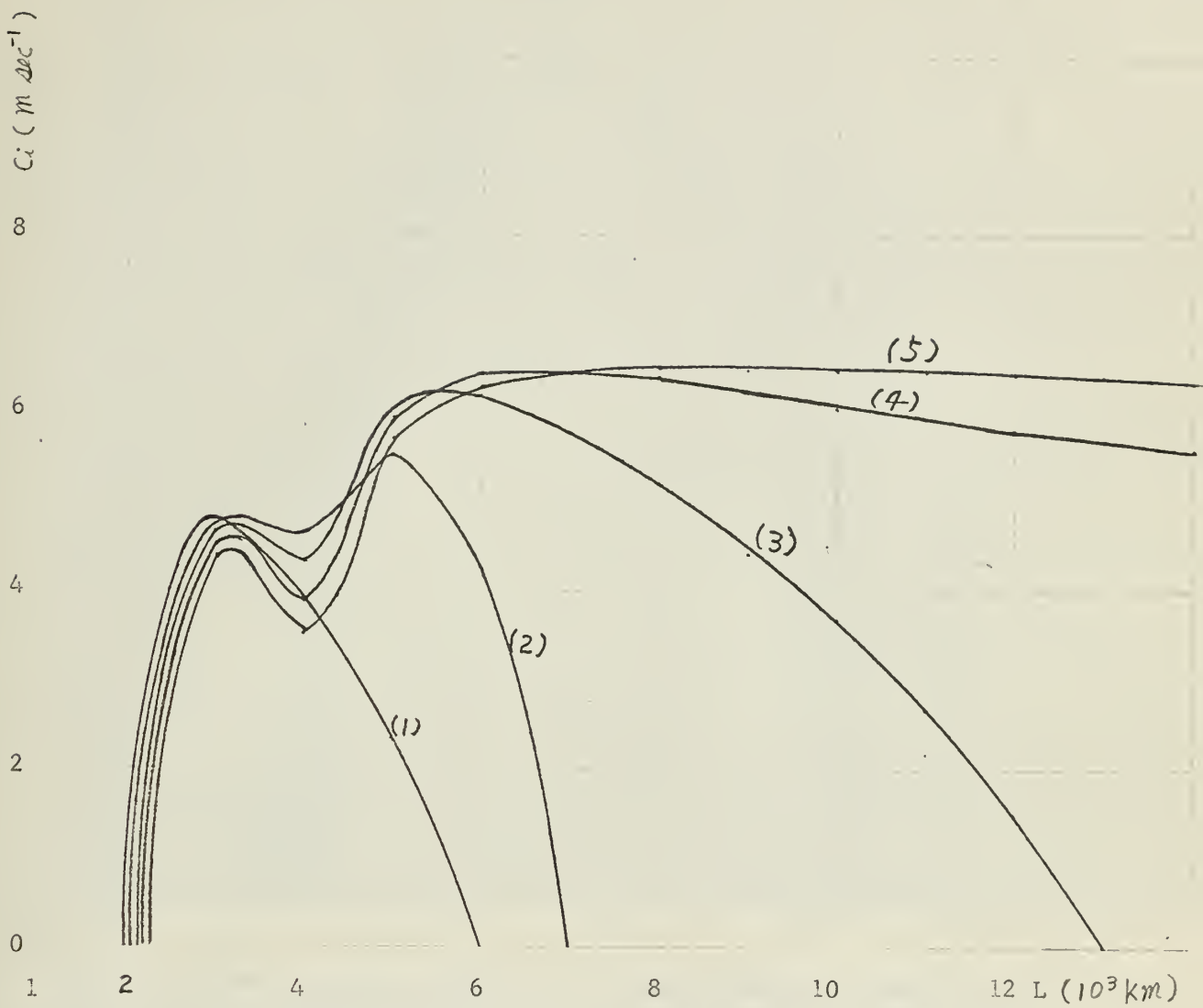


Fig. 12. The imaginary part,  $c_i$ , of the solution to equation (2.12) as a function of wavelength for the same parameters as in fig. 11 except  $D = 4000 \text{ km}$ . The curves as in fig. 3.



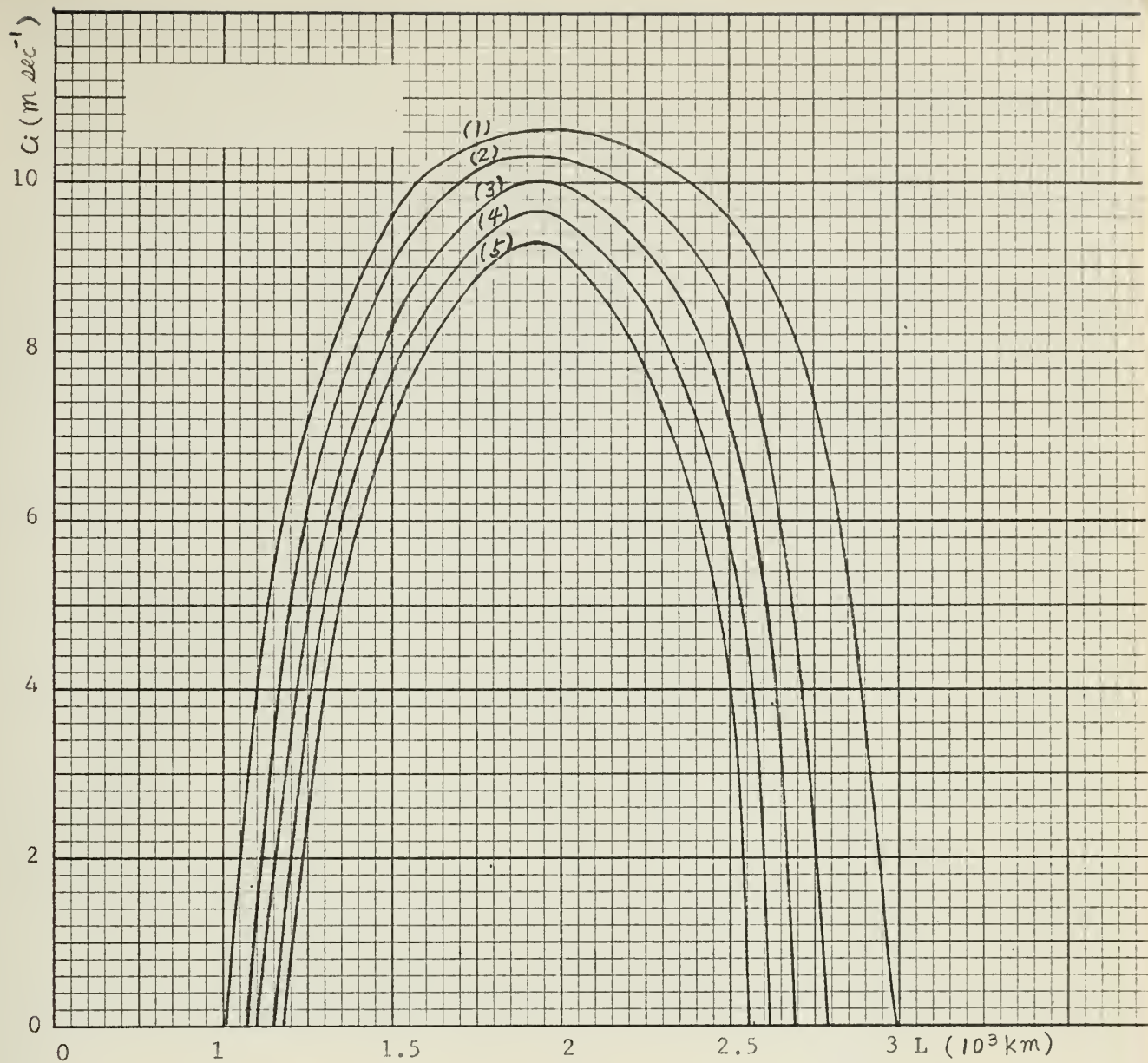


Fig. 13. The imaginary part,  $c_i$ , of the solution to equation (2.12) as a function of wavelength for  $U = B(\cos(4\pi y/D) - \cos(2\pi y/D))$ ,  $d = D/6$ ,  $D = 2000$  km, and  $B = 30$  m sec $^{-1}$ . The curves as in fig. 3.



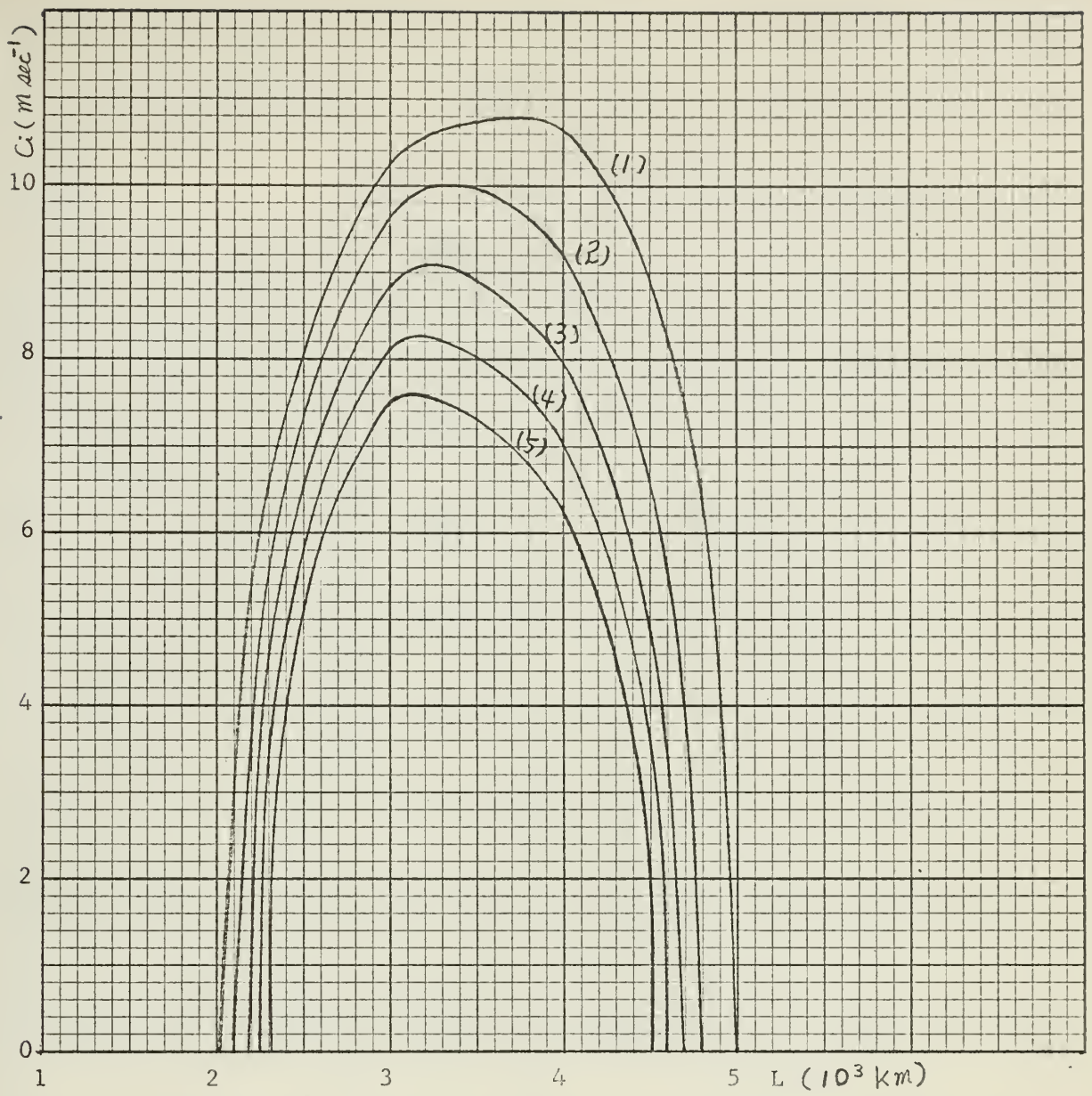


Fig. 14. The imaginary part,  $c_i$ , of the solution to equation (2.12) as a function of wavelength for the same parameters as in fig. 13 except  $D = 4000$  km. The curves as in fig. 3.





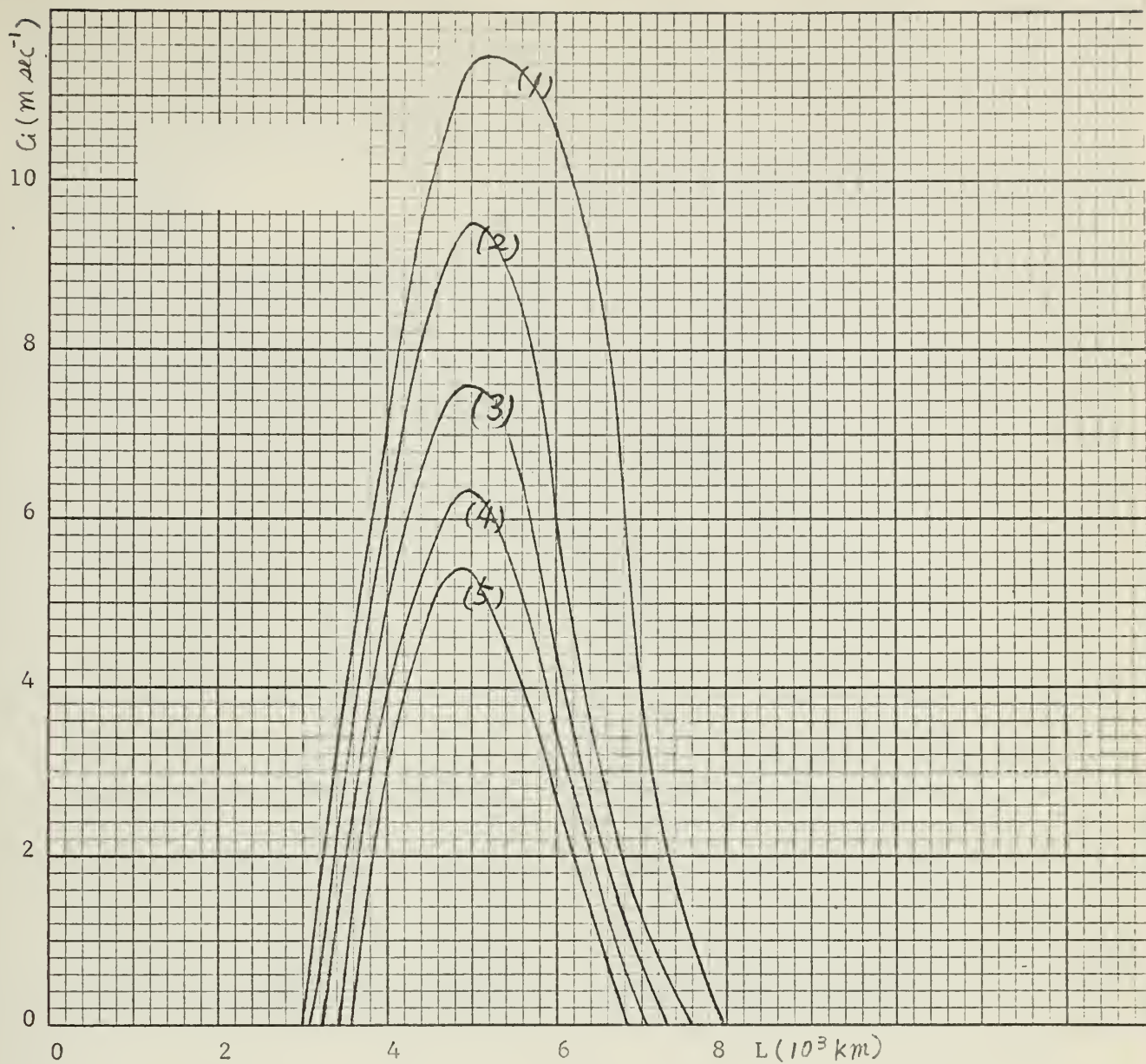


Fig. 15. The imaginary part,  $c_i$ , of the solution to equation (2.12) as a function of wavelength for the same parameters as in fig. 13 except  $D = 6000$  km. The curves as in fig. 3.



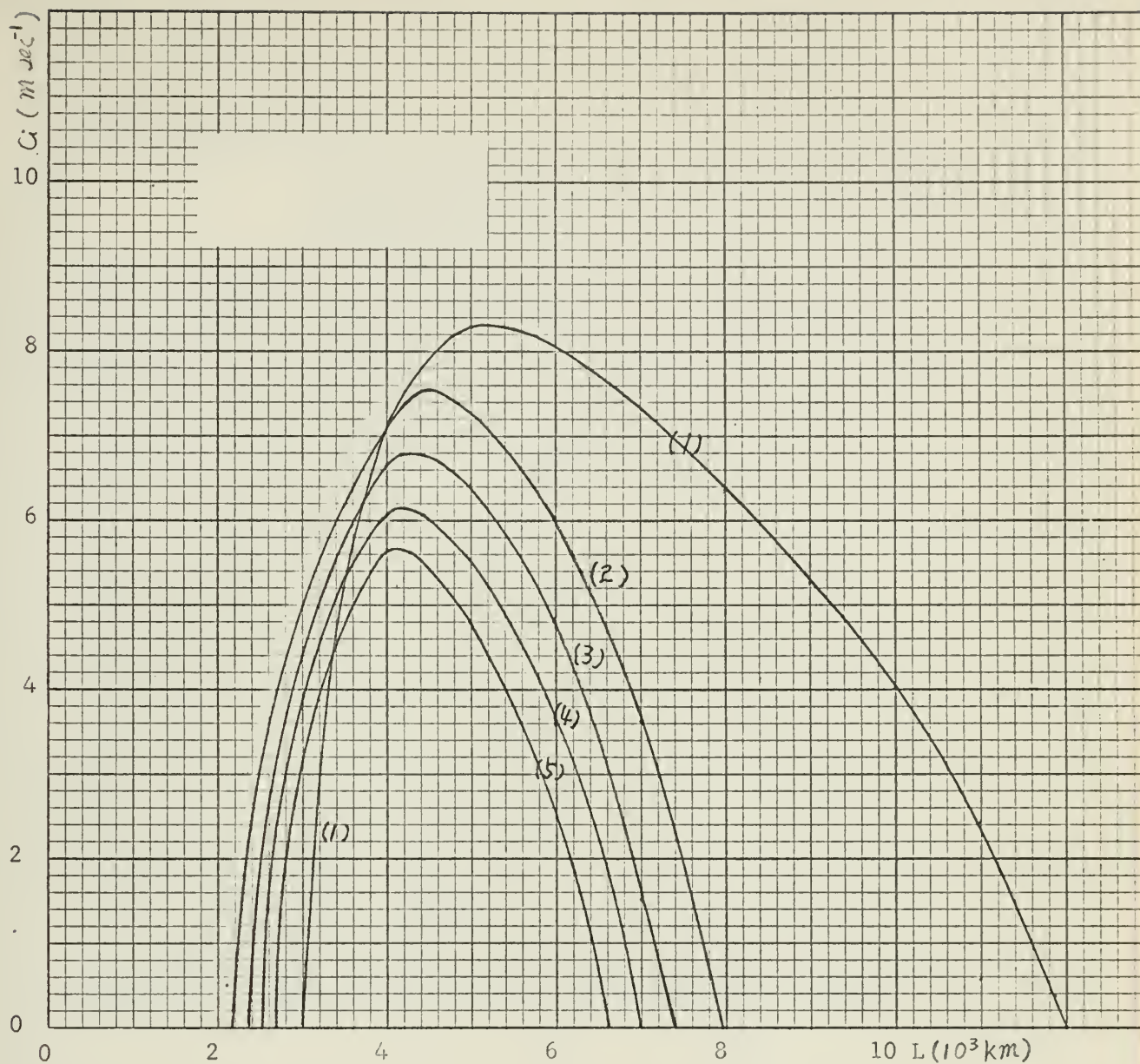


Fig. 17. The imaginary part,  $c_i$ , of the solution to equation (2.18) as a function of wavelength for  $U = B(1 - \cos(2\pi y/D))$ ,  $d = D/8$ ,  $D = 2000$  km, and  $B = 30$  m sec $^{-1}$ . The curves as in fig. 3.





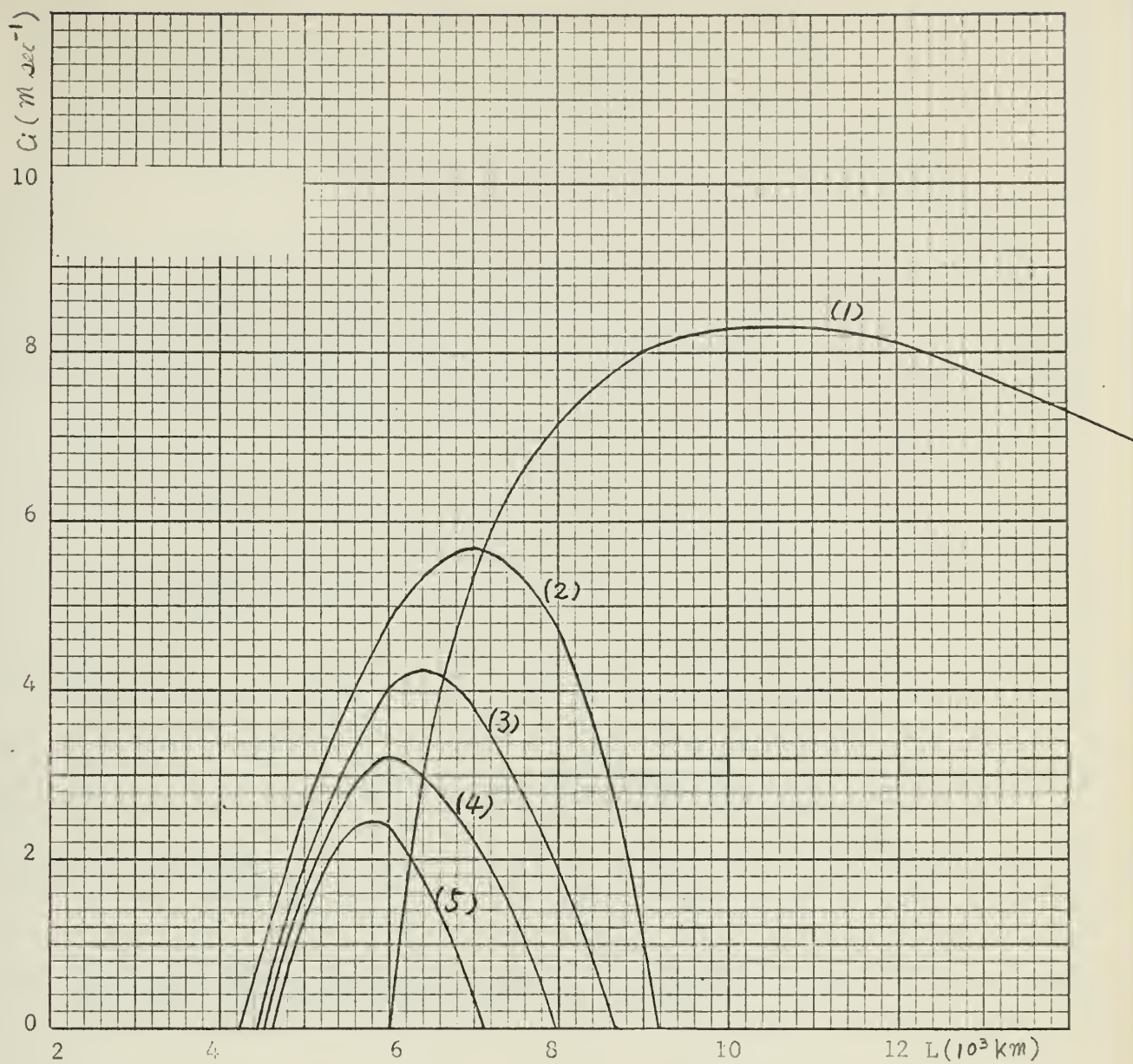


Fig. 13. The imaginary part,  $c_i$ , of the solution to equation (2.18) as a function of wavelength for the same parameters as in fig. 17 except  $D = 4000$  km. The curves as in fig. 3.



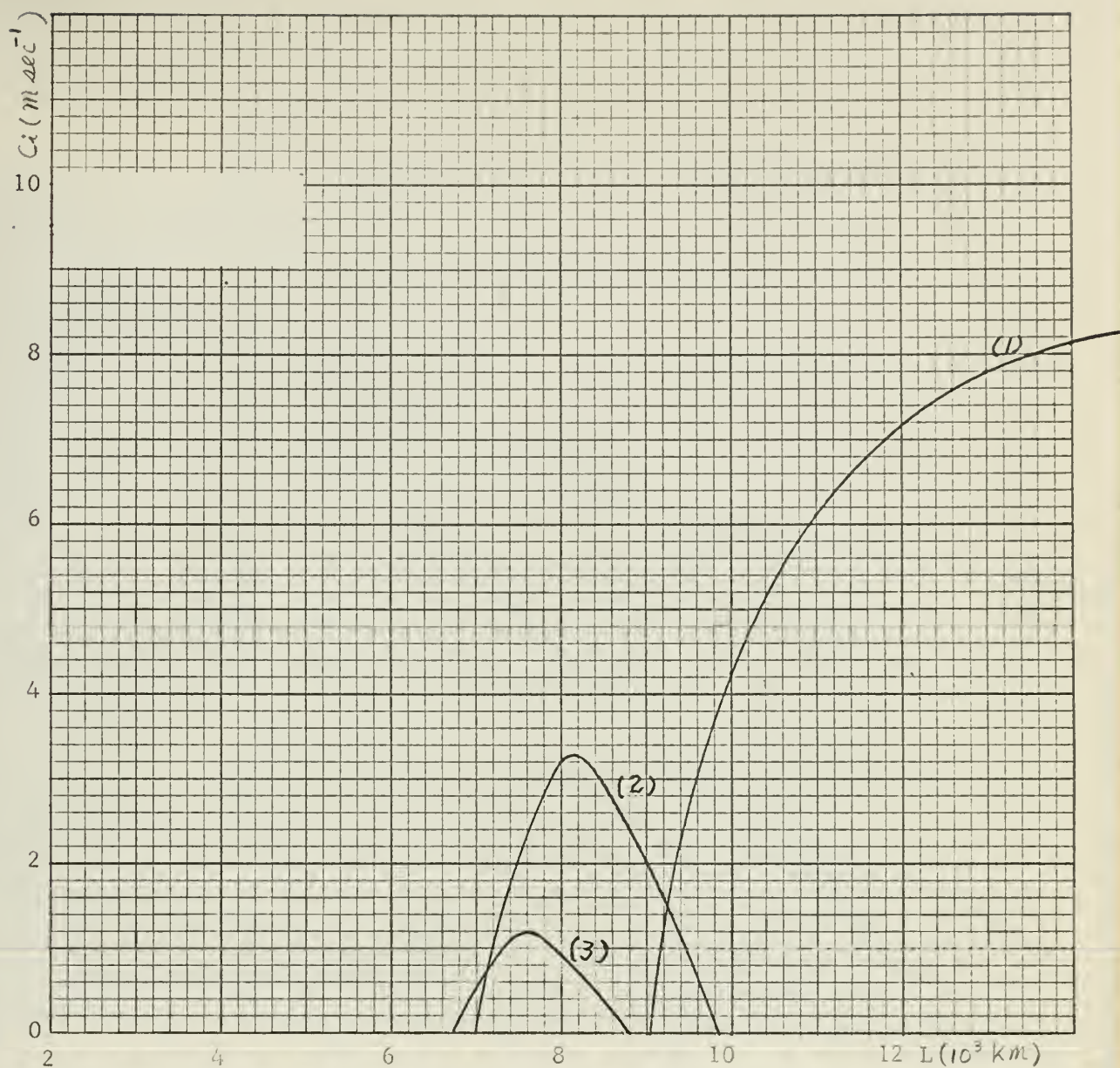


Fig. 19. The imaginary part,  $c_i$ , of the solution to equation (2.18) as a function of wavelength for the same parameters as in fig. 17 except  $D = 6000$  km. The curves as in fig. 3.





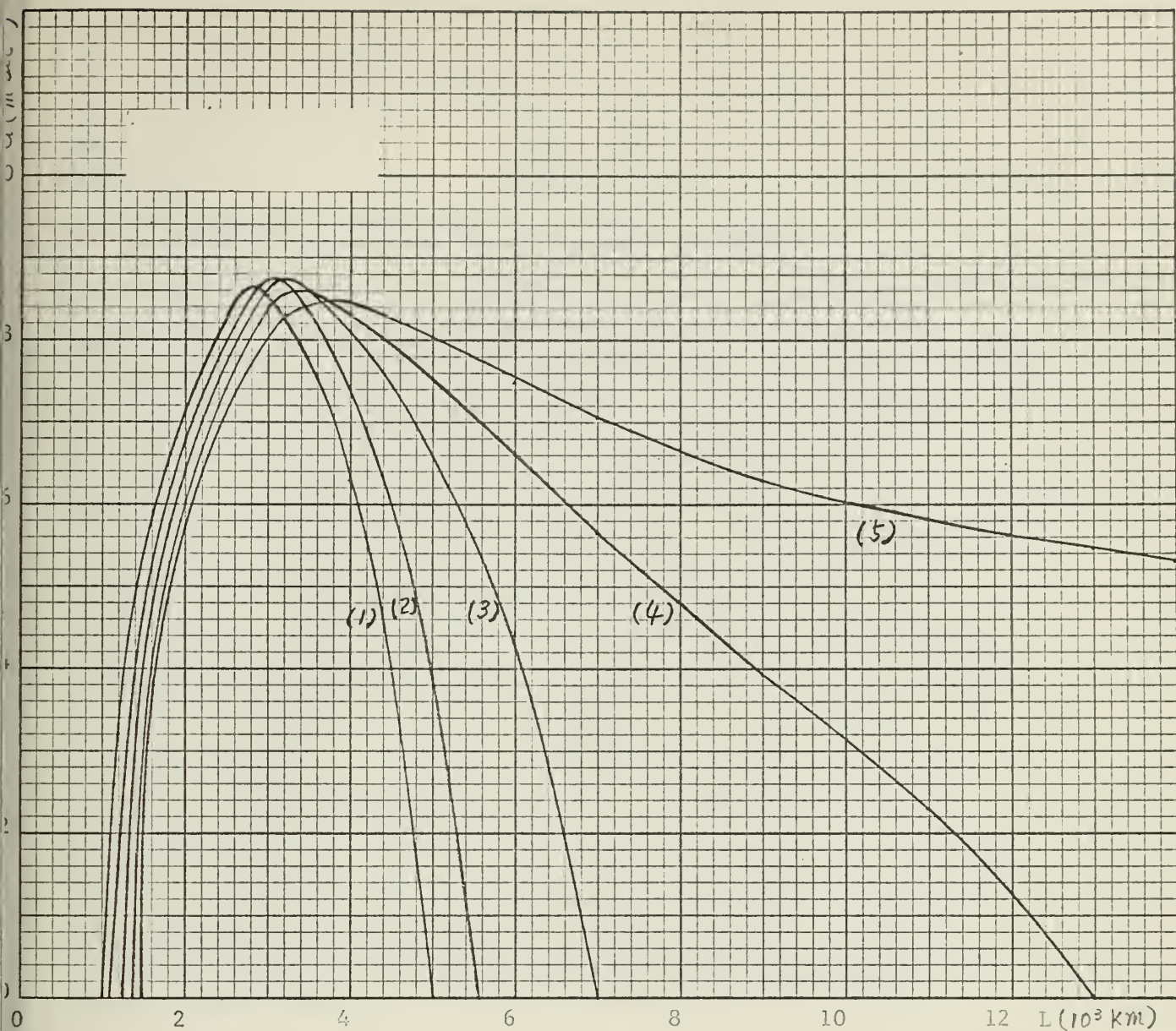


Fig. 20. The imaginary part,  $c_i$ , of the solution to equation (2.18) as a function of wavelength for  $U = B(\sin(\pi y/D) + \sin(3\pi y/D))$ ,  $d = D/8$ ,  $D = 2000$  km, and  $B = 40 \text{ m sec}^{-1}$ . The curves as in fig. 3.



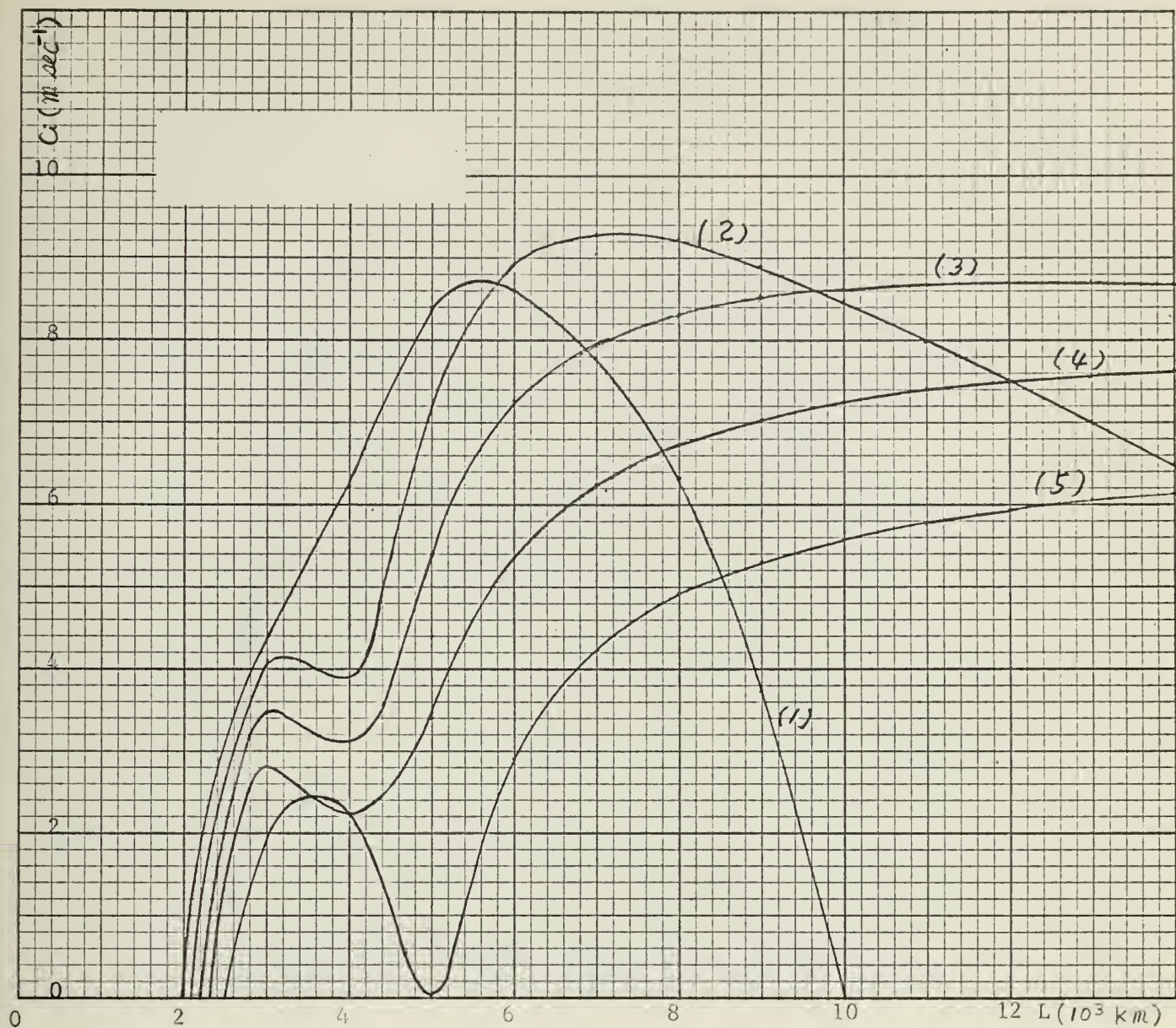


Fig. 21. The imaginary part,  $c_i$ , of the solution to equation (2.18) as a function of wavelength for the same parameters as in fig. 20 except  $D = 4000$  km. The curves as in fig. 3.





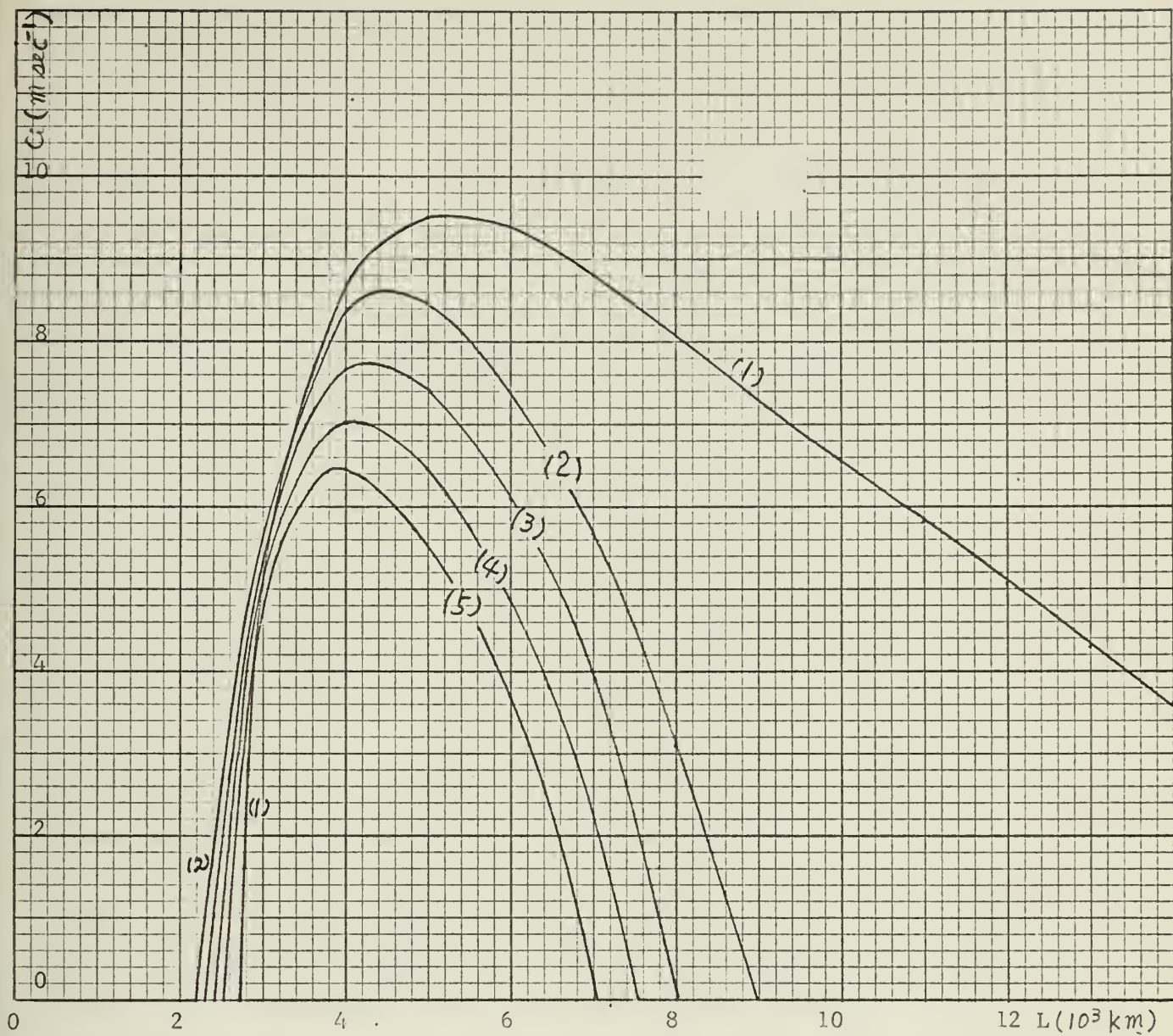


Fig. 22. The imaginary part,  $c_i$ , of the solution to equation (2.22) as a function of wavelength for  $U = B(1 - \cos(2\pi y/D))$ ,  $N = 5$ ,  $D = 2000$  km, and  $B = 30$  m sec<sup>-1</sup>. The curves as in fig. 3.



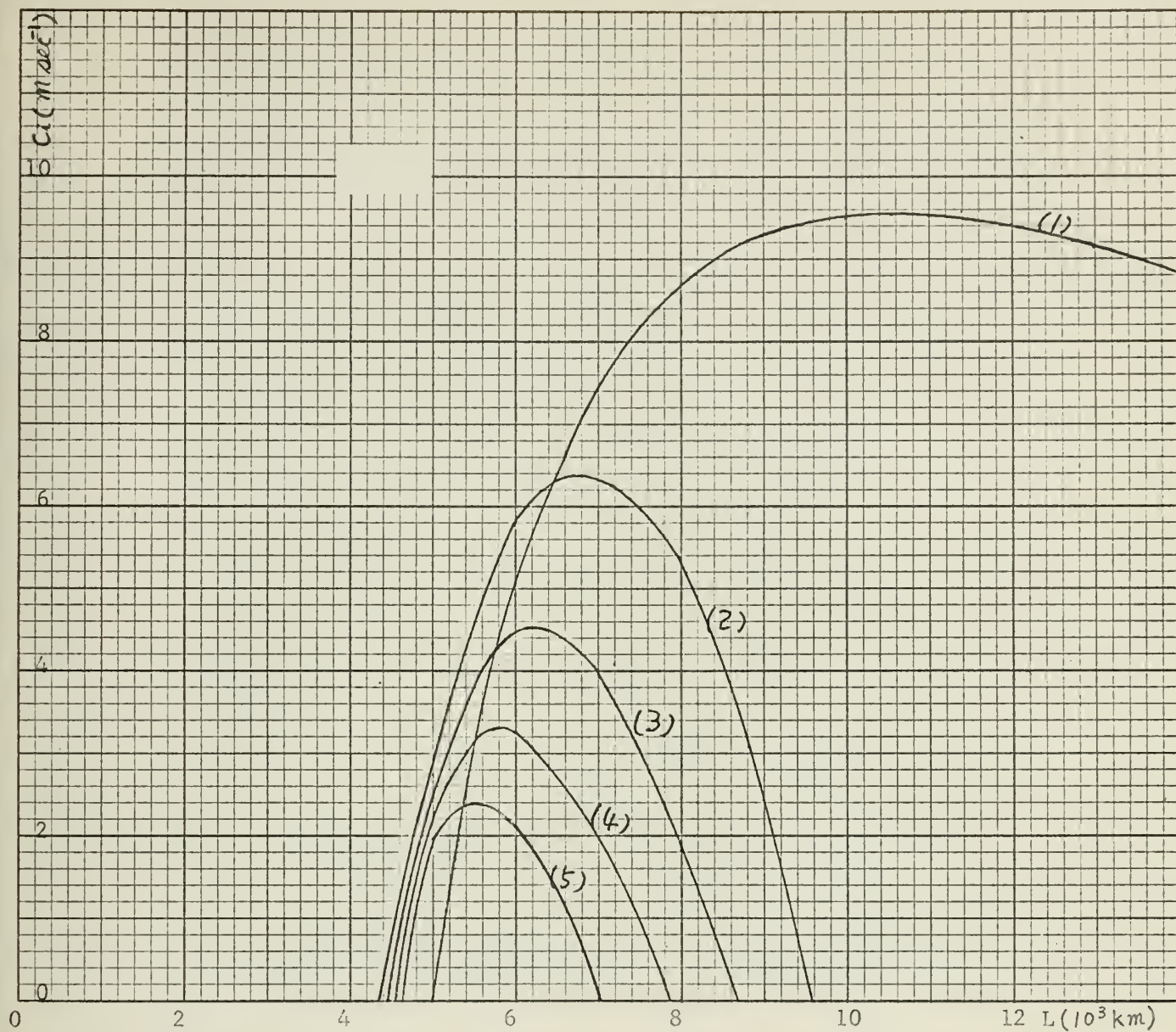


Fig. 23. The imaginary part,  $c_i$ , of the solution to equation (2.22) as a function of wavelength for the same parameters as in fig. 22 except  $D = 4000$  km. The curves as in fig. 3.





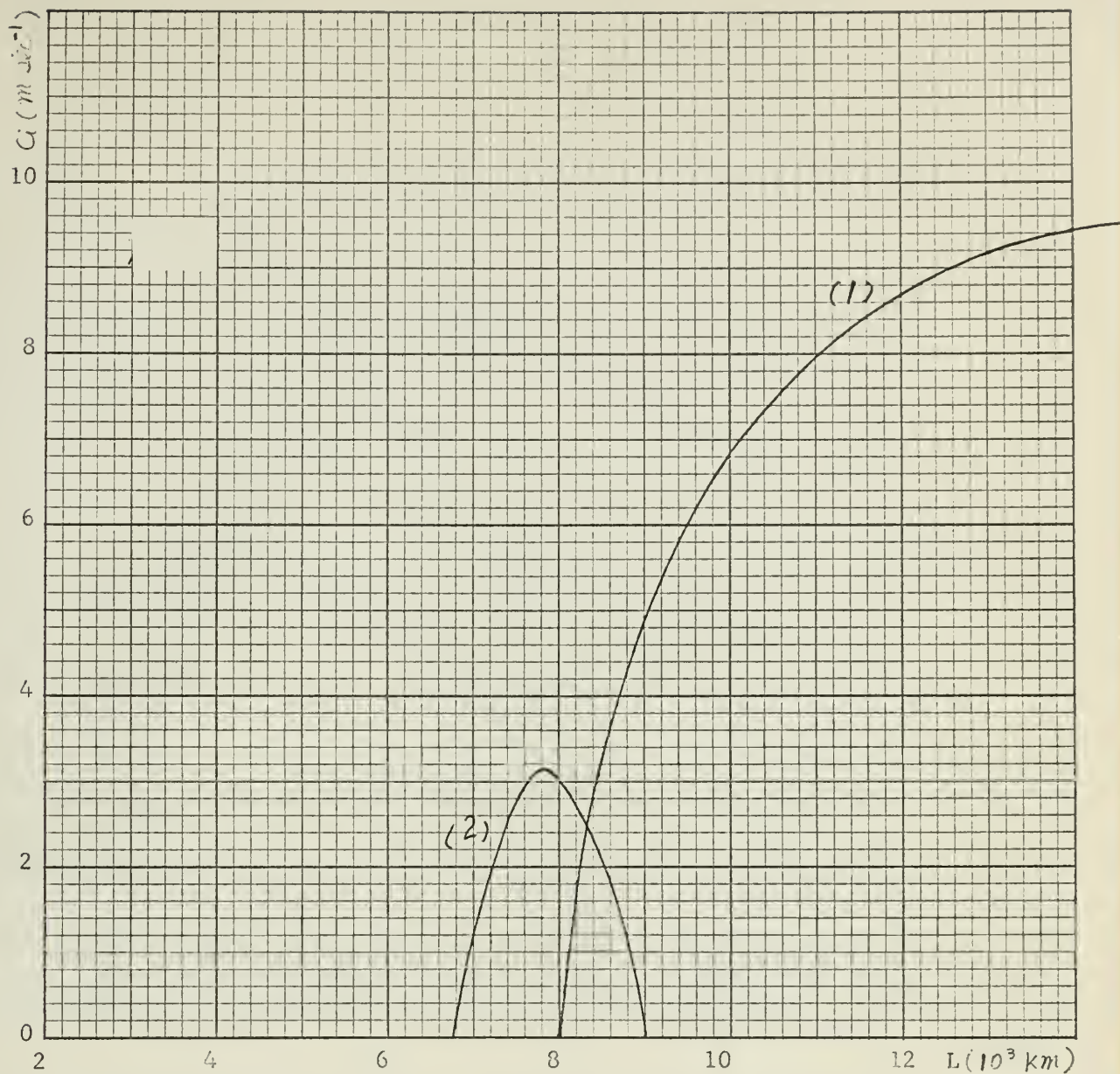


Fig. 24. The imaginary part,  $c_i$ , of the solution to equation (2.22) as a function of wavelength for the same parameters as in fig. 22 except  $D = 6000$  km. The curves (1) and (2) as in fig. 3.



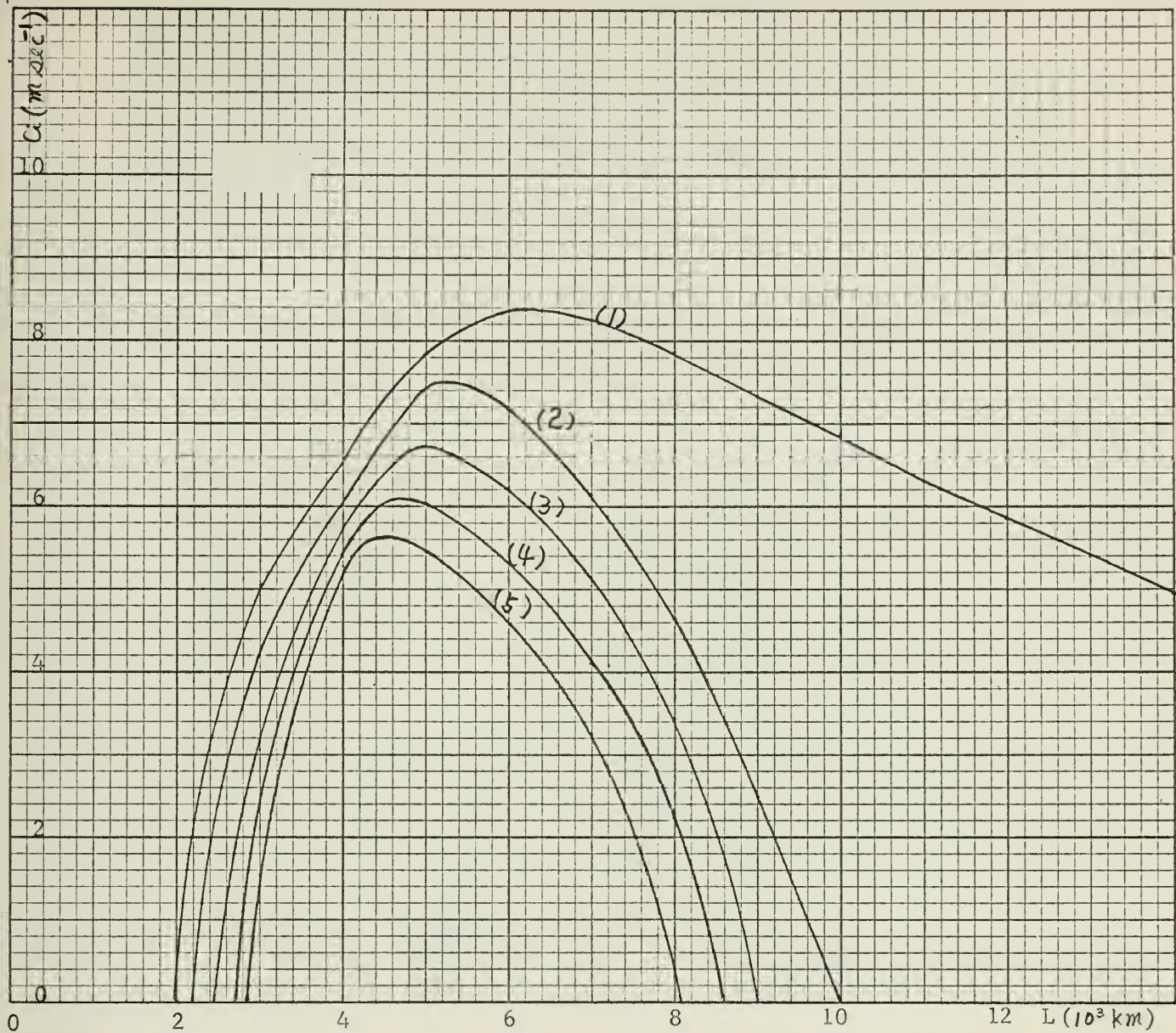


Fig. 25. The imaginary part,  $c_i$ , of the solution to equation (2.23) as a function of wavelength for the same parameters as in fig. 22 except  $N = 7$ . The curves as in fig. 3.





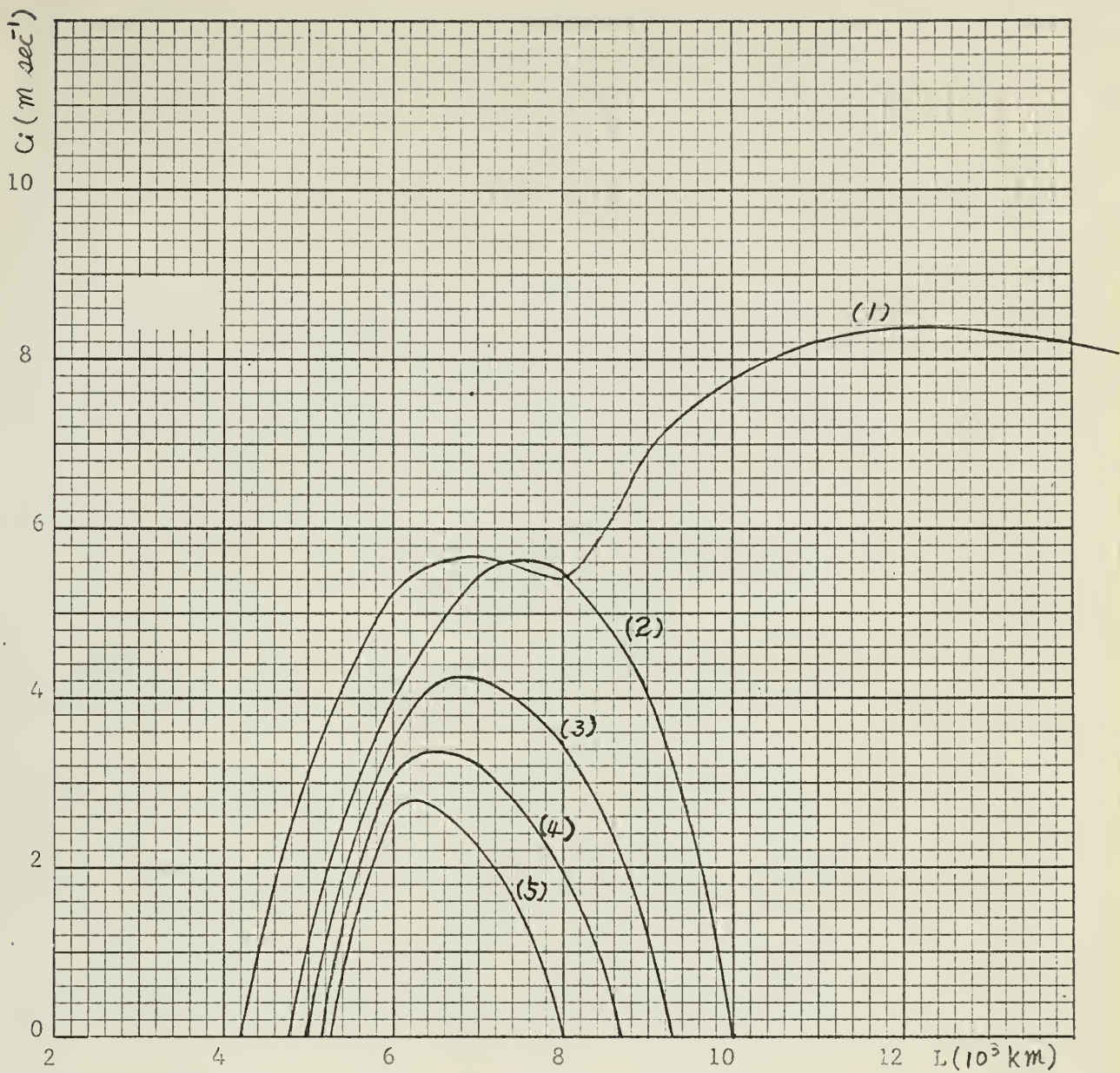


Fig. 26. The imaginary part,  $c_i$ , of the solution to equation (2.23) as a function of wavelength for the same parameters as in fig. 23 except  $N = 7$ . The curves as in fig. 3.



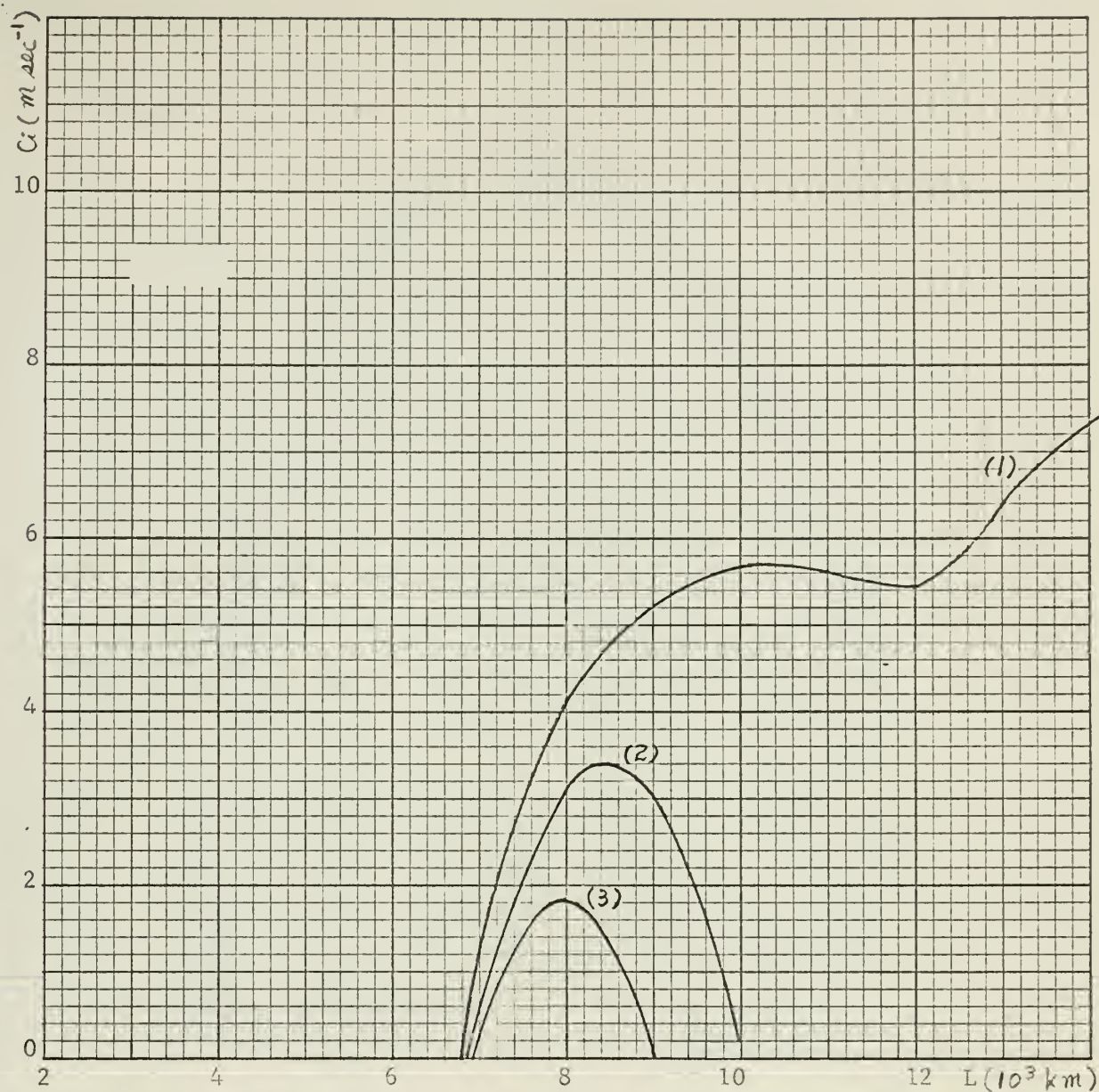


Fig. 27. The imaginary part,  $c_i$ , of the solution to equation (2.23) as a function of wavelength for the same parameters as in fig. 24 except  $N = 7$ . The curves as in fig. 3.





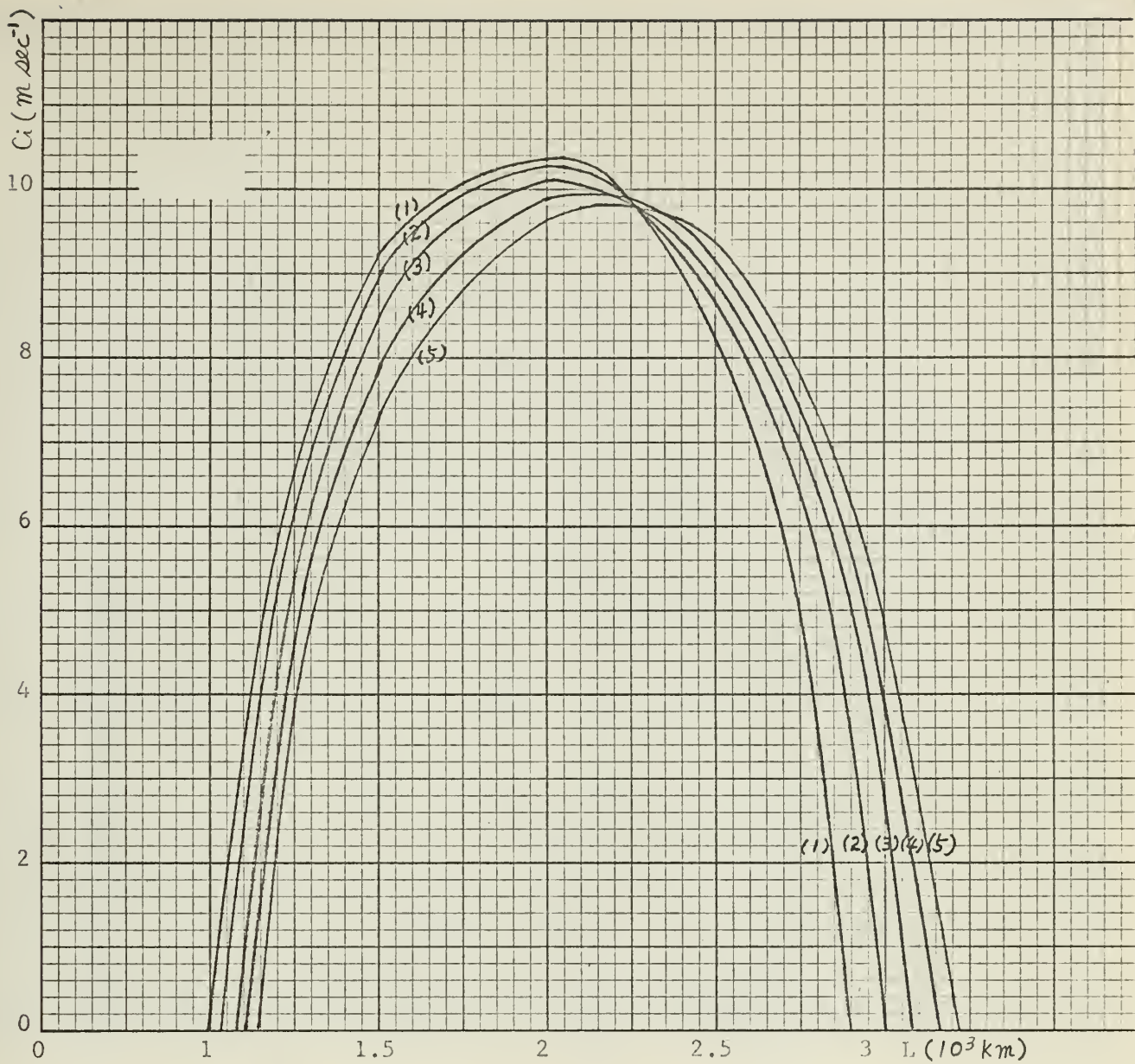


Fig. 28. The imaginary part,  $c_i$ , of the solution to equation (2.26) as a function of wavelength for  $U = B(1 - \cos(4\pi y/D))$ ,  $N = 5$ ,  $D = 2000$  km, and  $B = 30$  m sec $^{-1}$ . The curves as in fig. 3.



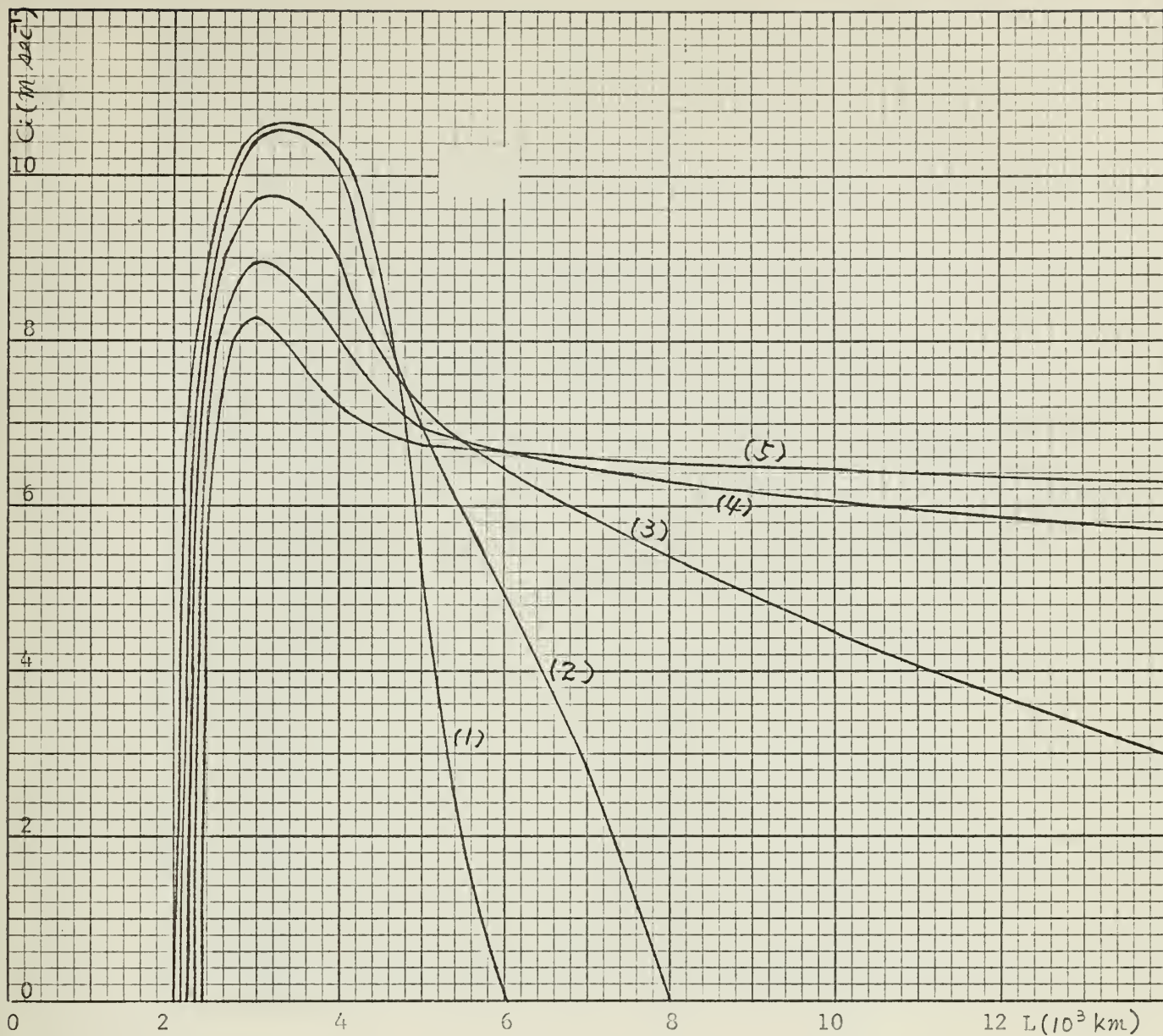


Fig. 29. The imaginary part,  $c_i$ , of the solution to equation (2.26) as a function of wavelength for the same parameters as in fig. 23 except  $D = 4000$  km. The curves as in fig. 3.





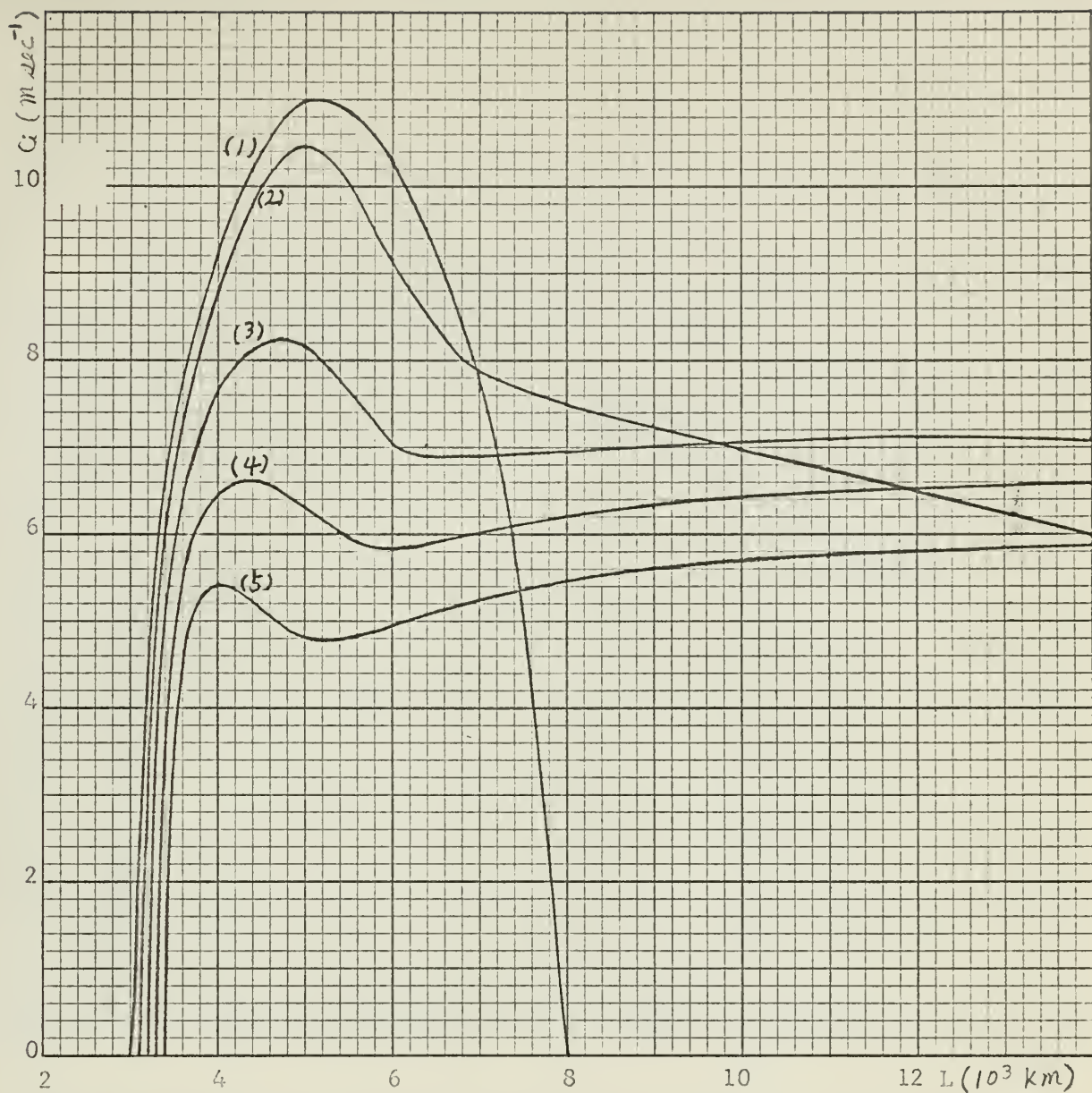


Fig. 30. The imaginary part,  $c_i$ , of the solution to equation (2.26) as a function of wavelength for the same parameters as in fig. 28 except  $D = 6000$  km. The curves as in fig. 3.



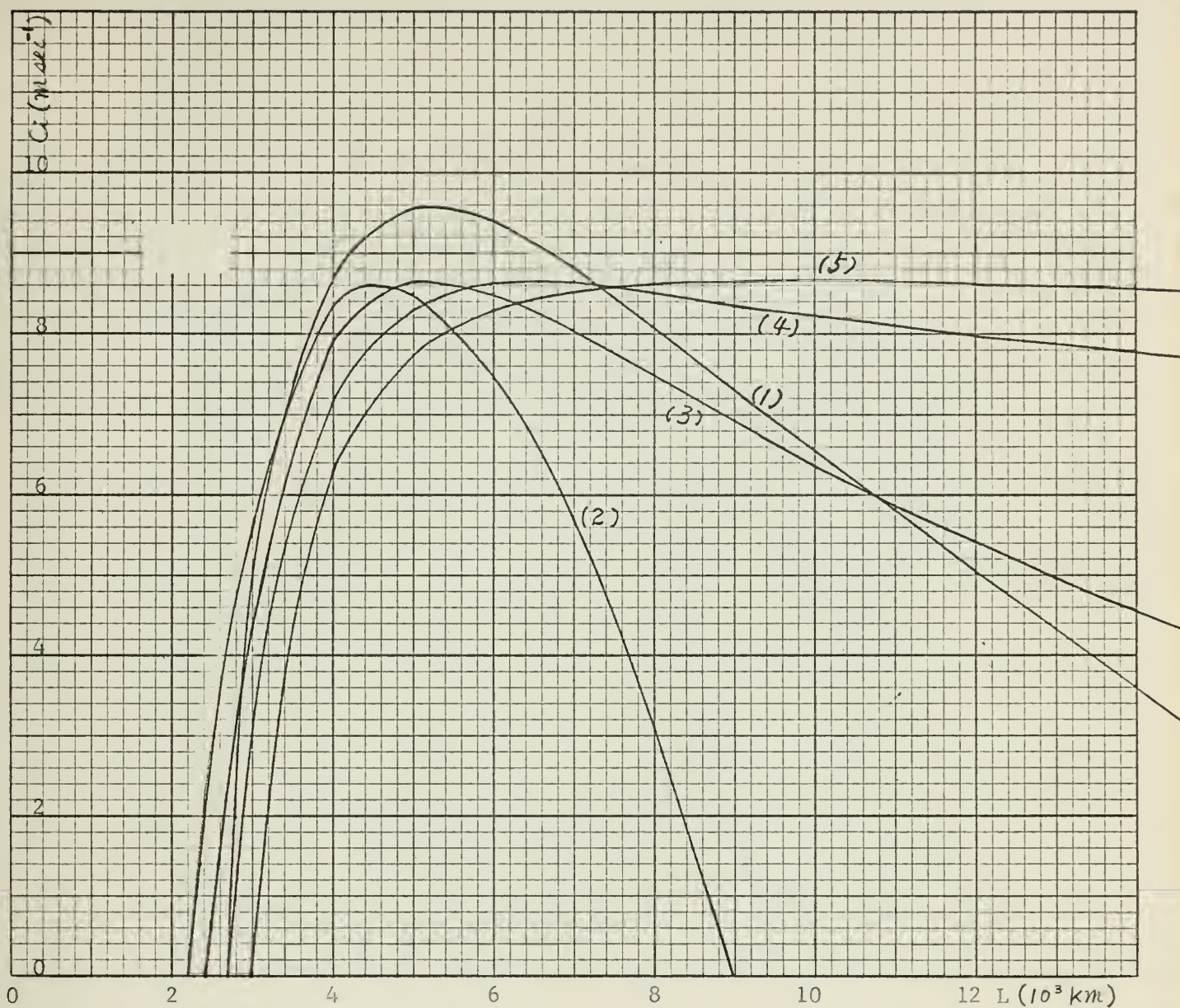


Fig. 31. The imaginary part,  $c_i$ , of the solution to equation (3.4) as a function of wavelength for the stratified model,  $\bar{U} = B(1 - \cos(2\pi y/D))$ ,  $N = 5$ ,  $D = 2000$  km, and  $B = 30$  m sec<sup>-1</sup>. The curves as in fig. 3.





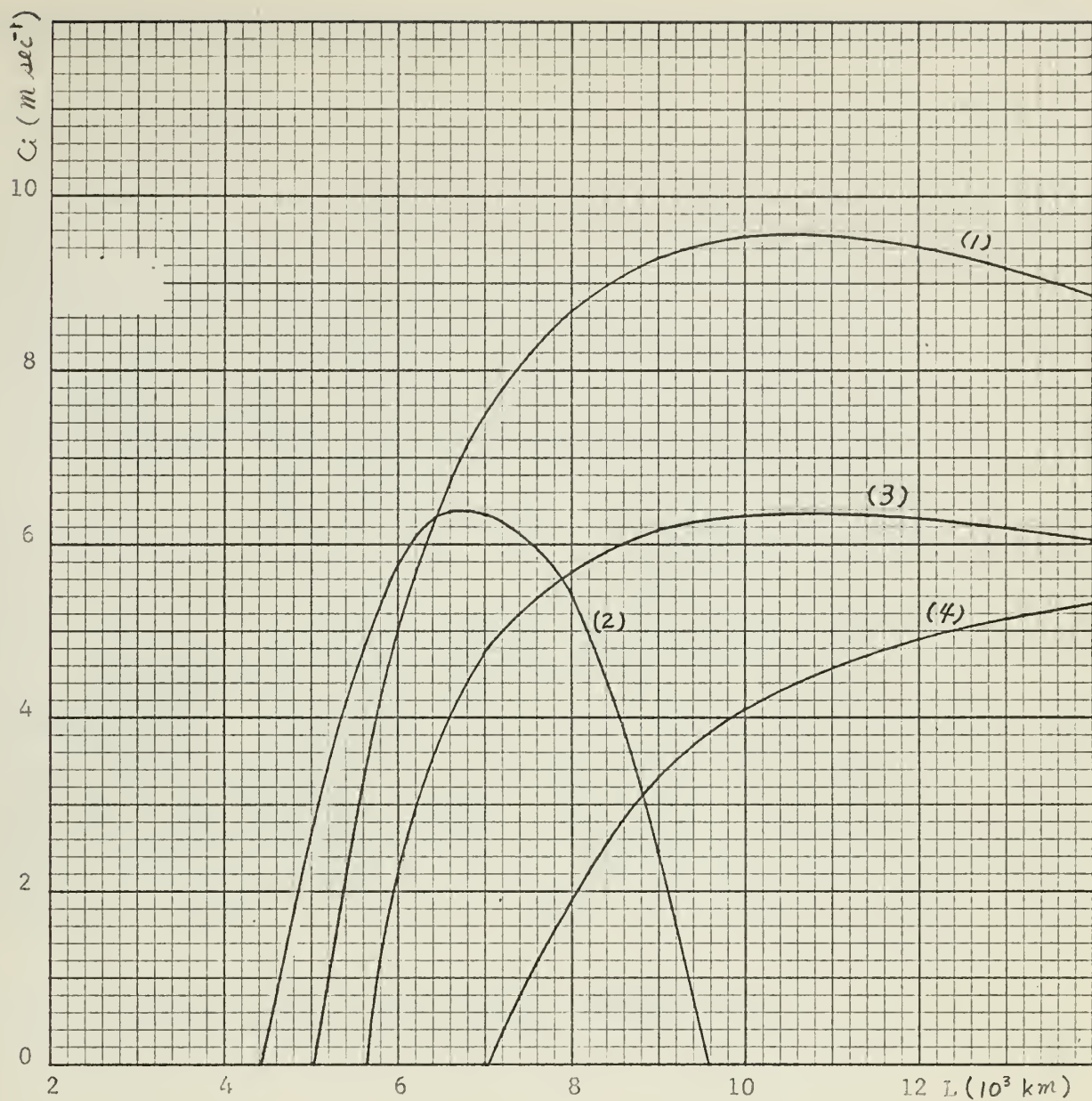


Fig. 32. The imaginary part,  $c_i$ , of the solution to equation (3.4) as a function of wavelength for the same parameters as in fig. 31 except  $D = 4000 \text{ km}$ . The curves as in fig. 3.



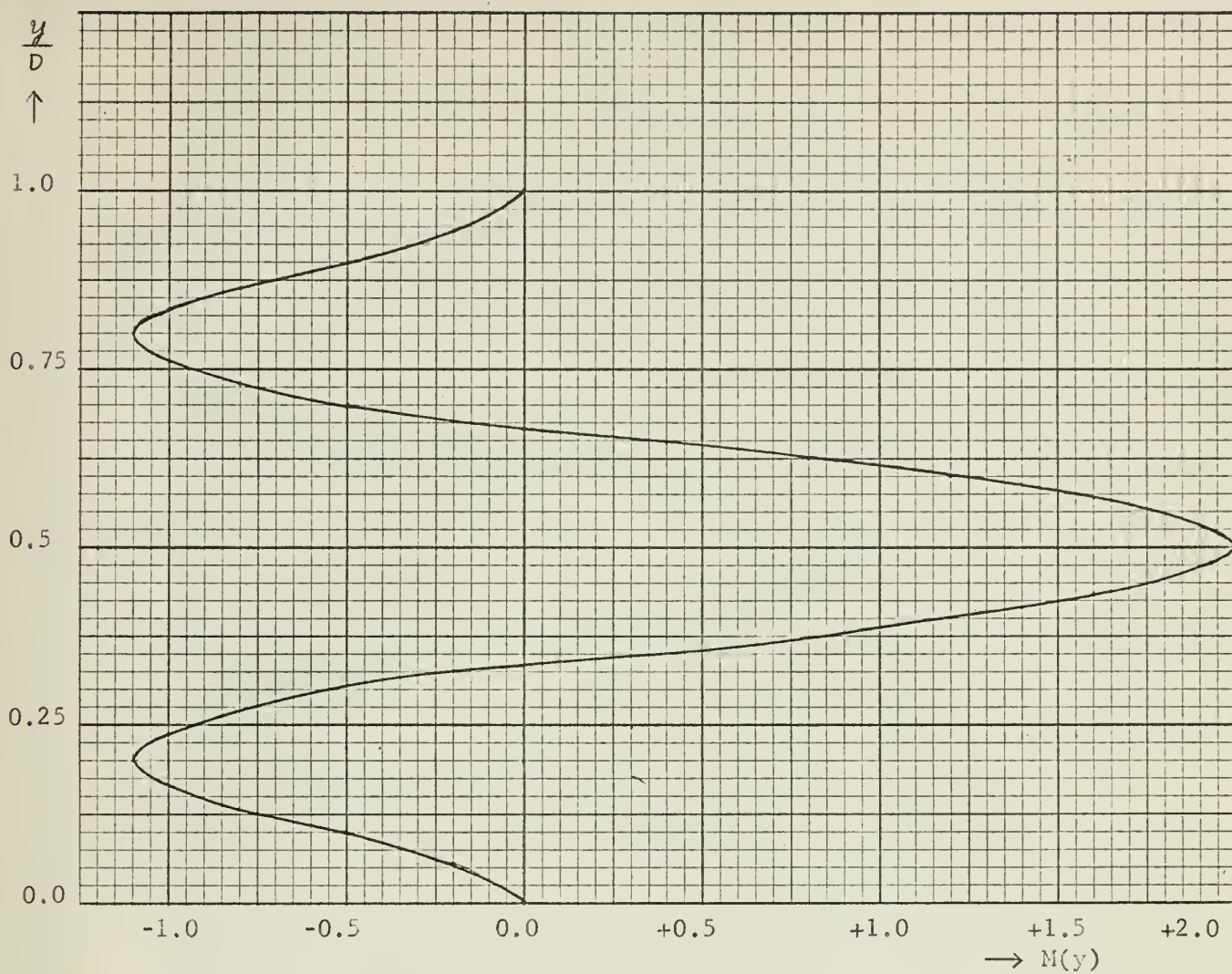


Fig. 33. The function  $M(y)$  as defined by equation (4.3).



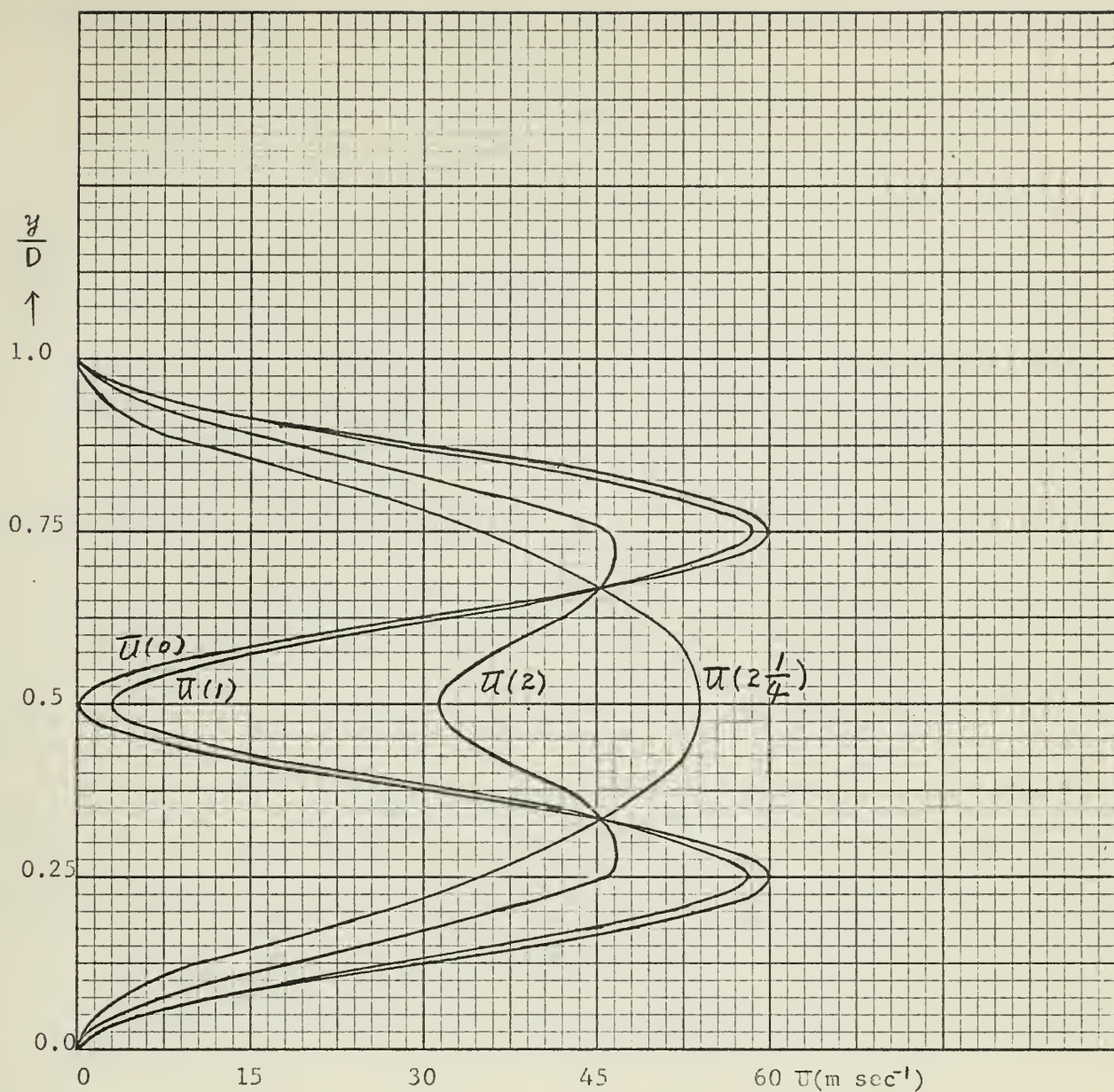


Fig. 34. The profiles of the zonal wind initially and at 1, 2, and  $2\frac{1}{4}$  days computed from equation (4.9) with  $\beta = \beta_{45}$ ,  $q^2 = 0$ ,  $L = 2000$  km,  $D = 3000$  km,  $B = 30$  m sec $^{-1}$ ,  $A_1$  corresponds to  $5$  m sec $^{-1}$  ( $1.59 \times 10^6$  m $^2$  sec $^{-1}$ ), and  $A_3 = 0$ .  $U(0) = B(1 - \cos(4\pi y/D))$ .





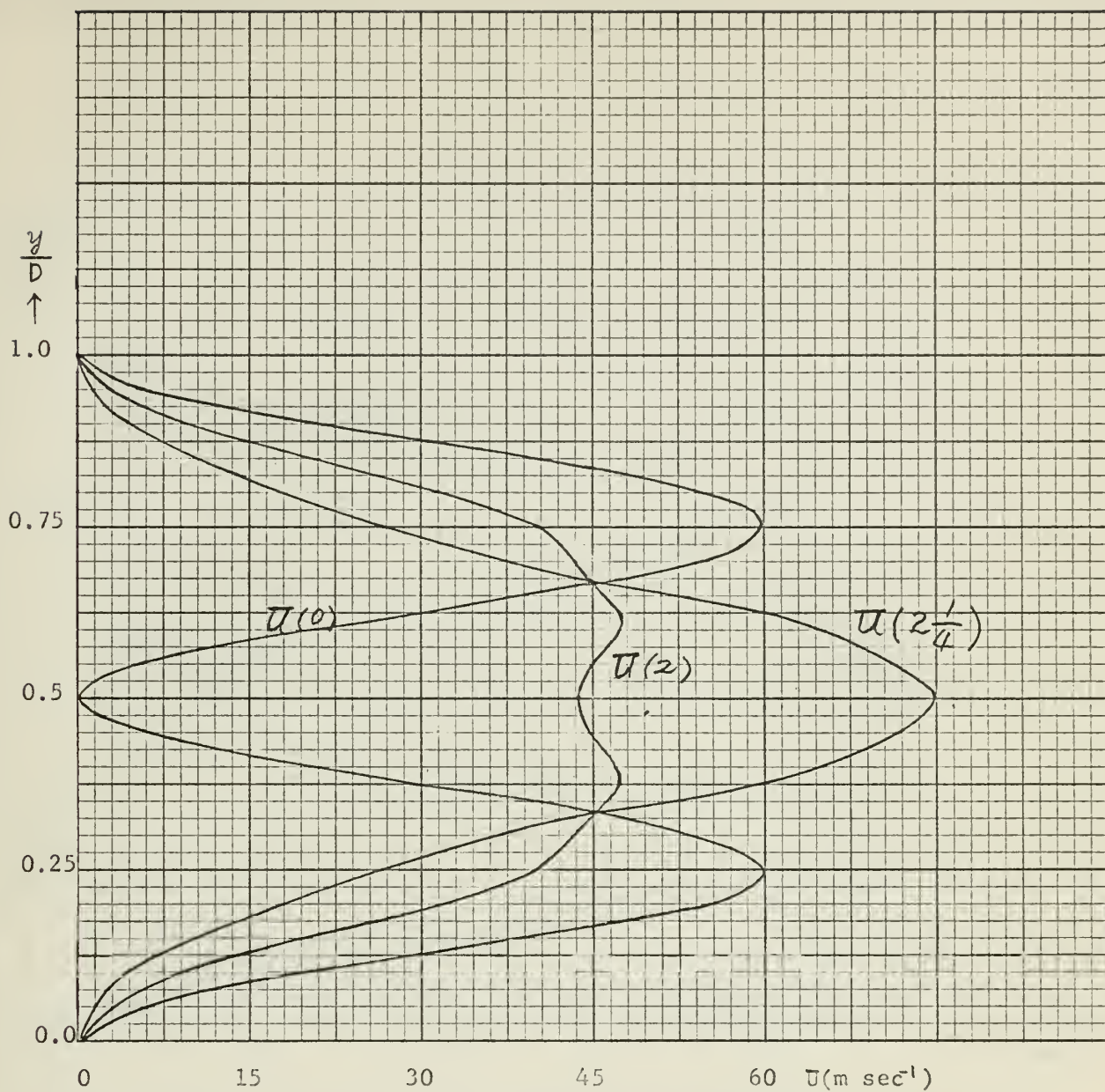


Fig. 35. The profiles of the zonal wind initially and at 2 and 2 1/4 days computed from equation (4.9) with parameters as in fig. 34 except  $A_3$  corresponding to  $5 \text{ m sec}^{-1}$  ( $A_3 = A_1$ ).





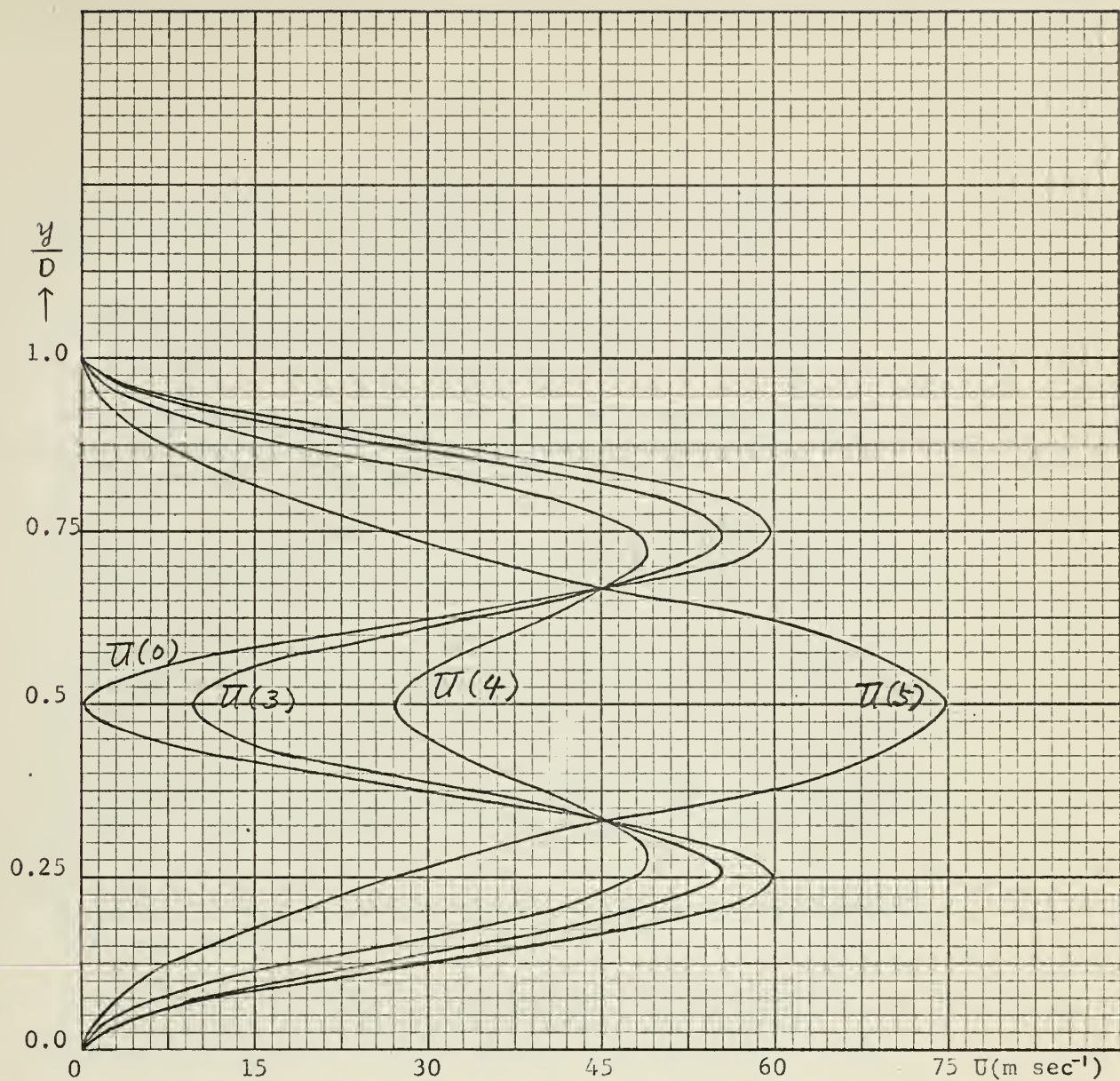


Fig. 36. The profiles of the zonal wind initially and at 3, 4, and 5 days computed from equation (4.9) with parameters as in fig. 35 except  $D = 6000$  km and  $L = 4000$  km.



# BIBLIOGRAPHY

1. Kuo, H. L., "Dynamic Instability of Two-Dimensional Non-Divergent Flow in a Barotropic Atmosphere", Journal of Meteorology, Vol. 6, No. 2, Apr. 1947, pp. 105-122.
2. Eliassen, E., "Numerical Solutions of the Perturbation Equation for Linear Flow", Tellus, Vol. 6, No. 2, May 1954, pp. 183-192.
3. Wiin-Nielsen, A., "On Short- and Long-Term Variations in Quasi-Barotropic Flow", Monthly Weather Review, Vol. 89, No. 11, November 1961, pp. 461-476.
4. Thompson, P.D., "A Heuristic Theory of Large-Scale Turbulence and Long-Period Velocity Variations in Barotropic Flow", Tellus, Vol. 9, No. 1, Feb. 1957, pp. 63-91.
5. Wiin-Nielsen, A., "On Barotropic and Baroclinic Models, with Special Emphasis on Ultra-Long Waves", Monthly Weather Review, Vol. 87, No. 5, May 1959, pp. 171-183.
6. Muller, D. E., "A Method for Solving Algebraic Equations using an Automatic Computer", Mathematical Tables and other Aids to Computation, Vol. 10, No. 56, Oct. 1956, pp. 203-215.
7. Thompson, P. D., "Numerical Weather Analysis and Prediction", 1961, pp. 110-114.
8. Arnason, G., "A Study of the Dynamics of a Stratified Fluid in Relation to Atmospheric Motions and Physical Weather Prediction", Project NAWEP, U.S. Navy, Dec. 1960.







0023 62

BINDERY  
BINDERY

Thesis

57048

S66563

Song

Stability character-  
istics of quasi-baro-  
tropic flow.

BINDERY

Thesis

57048

S66563

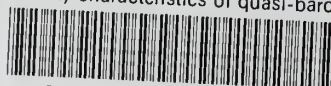
Song

Stability character-  
istics of quasi-baro-  
tropic flow.



thesS66563

Stability characteristics of quasi-barot



3 2768 002 01683 4

DUDLEY KNOX LIBRARY